

# Geochemistry, Geophysics, Geosystems

## RESEARCH ARTICLE

10.1029/2020GC009585

### Key Points:

- The tectonic migration of ocean floor led to a transition from an organic carbon-starved to an elevated organic carbon burial environment
- Diagenetic transformation of iron oxides into pyrite within the carbon-lean sediments occurred several millions of years after deposition
- Reducible iron(III), which is mostly present in phyllosilicates, can potentially fuel microbially mediated mineral alteration

### Supporting Information:

Supporting Information may be found in the online version of this article.

### Correspondence to:

M. Köster,  
[male.koester@awi.de](mailto:male.koester@awi.de)

### Citation:












Köster, M., Kars, M., Schubotz, F., Tsang, M.-Y., Maisch, M., Kappler, A., et al. (2021). Evolution of (bio-)geochemical processes and diagenetic alteration of sediments along the tectonic migration of ocean floor in the Shikoku Basin off Japan. *Geochemistry, Geophysics, Geosystems*, 22, e2020GC009585. <https://doi.org/10.1029/2020GC009585>

Received 7 DEC 2020  
 Accepted 17 JUN 2021

© 2021. The Authors.

This is an open access article under the terms of the [Creative Commons Attribution License](https://creativecommons.org/licenses/by/4.0/), which permits use, distribution and reproduction in any medium, provided the original work is properly cited.

## Evolution of (Bio-)Geochemical Processes and Diagenetic Alteration of Sediments Along the Tectonic Migration of Ocean Floor in the Shikoku Basin off Japan

Male Köster<sup>1</sup> , Myriam Kars<sup>2</sup> , Florence Schubotz<sup>3</sup> , Man-Yin Tsang<sup>4,5</sup> , Markus Maisch<sup>6</sup> , Andreas Kappler<sup>6,7</sup> , Yuki Morono<sup>8</sup> , Fumio Inagaki<sup>8,9</sup> , Verena B. Heuer<sup>3</sup> , Sabine Kasten<sup>1,3,10</sup> , and Susann Henkel<sup>1,3</sup> 

<sup>1</sup>Alfred Wegener Institute Helmholtz Centre for Polar and Marine Research, Bremerhaven, Germany, <sup>2</sup>Center for Advanced Marine Core Research, Kochi University, Nankoku, Japan, <sup>3</sup>MARUM—Center for Marine Environmental Sciences, University of Bremen, Bremen, Germany, <sup>4</sup>Department of Applied Earth Sciences, University of Toronto, Toronto, ON, Canada, <sup>5</sup>Now at Department of Planetology, Kobe University, Kobe, Japan, <sup>6</sup>Center for Applied Geosciences, University of Tübingen, Tübingen, Germany, <sup>7</sup>Center for Geomicrobiology, Aarhus University, Aarhus, Denmark, <sup>8</sup>Kochi Institute for Core Sample Research, Japan Agency for Marine-Earth Sciences and Technology (JAMSTEC), Nankoku, Japan, <sup>9</sup>Mantle Drilling Promotion Office (MDP), Institute for Marine-Earth Exploration and Engineering (MarE3), Japan Agency for Marine-Earth Science and Technology (JAMSTEC), Yokohama, Japan, <sup>10</sup>University of Bremen, Faculty of Geosciences, Bremen, Germany

**Abstract** Biogeochemical processes in subseafloor sediments are closely coupled to global element cycles. To improve the understanding of changes in biogeochemical conditions on geological timescales, we investigate sediment cores from a 1,180 m deep hole in the Nankai Trough offshore Japan (Site C0023) drilled during International Ocean Discovery Program Expedition 370. During its tectonic migration from the Shikoku Basin to the Nankai Trough over the past 15 Ma, Site C0023 has experienced significant changes in depositional, thermal, and geochemical conditions. By combining pore-water, solid-phase, and rock magnetic data, we demonstrate that a transition from organic carbon-starved conditions with predominantly aerobic respiration to an elevated carbon burial environment with increased sedimentation occurred at ~2.5 Ma. Higher rates of organic carbon burial in consequence of increased nutrient supply and productivity likely stimulated the onset of anaerobic electron-accepting processes during organic carbon degradation. A significant temperature increase by ~50°C across the sediment column associated with trench-style sedimentation since ~0.5 Ma could increase the bioavailability of organic matter and enhance biogenic methanogenesis. The resulting shifts in reaction fronts led to diagenetic transformation of iron (oxyhydr)oxides into pyrite in the organic carbon-starved sediments several millions of years after burial. We also show that high amounts of reducible iron(III) which can serve as electron acceptor for microbial iron(III) reduction are preserved and still available as phyllosilicate-bound iron. This is the first study that shows the evolution of long-term variations of (bio-)geochemical processes along tectonic migration of ocean floor, thereby altering the primary sediment composition long after deposition.

**Plain Language Summary** During the tectonic migration of ocean floor, deep sediments move over vast distances, thereby passing through different depositional and geochemical environments. We studied subseafloor sediments recovered at Site C0023 in the Nankai Trough offshore Japan during International Ocean Discovery Program Expedition 370, which aimed at exploring the prerequisites and limits of microbial life in marine sediments. Over the past 15 Ma, the sediments at Site C0023 migrated ~750 km from its initial position to the Nankai Trough due to tectonic motion of the Philippine Sea plate. As a result, sedimentation rates and sediment temperature increased significantly. We use different geochemical and rock magnetic analyses to (1) reconstruct the evolution of (bio-)geochemical processes, especially iron cycling, along the migration and to (2) investigate if iron(III) minerals are available to serve as energy substrates for microbial respiration in the deep sediments. Our results indicate that high amounts of phyllosilicate-bound iron(III), which can be used by microbes to gain energy, are still available throughout the core. The changing depositional history, and consequently the organic carbon availability and temperature, ultimately determine the geochemical patterns we observe today. Such studies are needed to gain a better understanding of changes in (bio-)geochemical cycling on geological timescales.

## 1. Introduction

The degradation of organic matter is the key driver for microbial activity and global biogeochemical cycles in subseafloor sediments (e.g., Berner, 1981; D'Hondt et al., 2002; Froelich et al., 1979). During burial, marine sediments pass through a sequence of geochemically and microbially determined redox zones (e.g., Berner, 1981; Froelich et al., 1979). In anoxic marine sediments, organic matter is predominantly remineralized by microbial dissimilatory iron (Fe) and sulfate reduction (e.g., Bowles et al., 2014; Canfield et al., 1993; Froelich et al., 1979; Jørgensen & Kasten, 2006), thus, linking the biogeochemical cycles of Fe, sulfur (S), and carbon (C). Hydrogen sulfide released during organoclastic sulfate reduction (e.g., Goldhaber & Kaplan, 1974; Jørgensen, 1982) or anaerobic oxidation of methane (AOM) (e.g., Barnes & Goldberg, 1976; Boetius et al., 2000; Borowski et al., 1996; Niewöhner et al., 1998) reacts with either solid-phase Fe(III) (oxyhydr)oxides or dissolved  $\text{Fe}^{2+}$  liberated by dissimilatory Fe(III) reduction to form Fe monosulfides (FeS) and/or pyrite ( $\text{FeS}_2$ ) (e.g., Berner, 1970; Jørgensen & Kasten, 2006; Jørgensen et al., 2019). The formation of Fe sulfides represents a long-term sink for Fe and S in deeply buried sediments (e.g., Berner, 1984; Hensen et al., 2003). Fe(III) reduction is considered one of the most ancient forms of microbial respiration (Vargas et al., 1998) and Fe(III)-reducing microorganisms can grow under high temperature and pressure conditions (Kashefi & Lovley, 2003). These findings suggest that microbes which use Fe(III) as electron acceptors are potential candidates to survive burial into deep and hot subseafloor sediments, as long as reducible Fe(III)-containing minerals are available.

Sequential extraction procedures are widely applied to marine sediments to quantify reactive Fe (e.g., Henkel et al., 2018; März et al., 2008; Riedinger et al., 2005, 2014). The extraction protocol after Poulton and Canfield (2005) is one of the most commonly utilized procedures for the selective dissolution of Fe in operationally defined fractions by using specific extracting reagents and reaction times. Despite the operational nature of the sequential extractions, this method has been developed through tests on pure and synthetic Fe-bearing minerals. Recent studies showed that substantial amounts of Fe from distinct phases can already be dissolved prior to the target extraction step and/or the dissolution can be incomplete (e.g., Henkel et al., 2016; Hepburn et al., 2020; Slotznick et al., 2020). Thus, if the research question requires a specific Fe mineral characterization, the extraction data should be validated by a secondary method (Hepburn et al., 2020; Slotznick et al., 2020). One option to assess the Fe mineralogy is  $^{57}\text{Fe}$ -specific Mössbauer spectroscopy, which is, however, relatively time-consuming. Another approach that offers independent information on Fe mineralogy is the application of comparably rapid and non-destructive magnetic techniques such as end-member modeling of isothermal remanent magnetization (IRM) acquisition curves. The basic principle of this method is to “unmix” the coercivity distributions of different magnetic minerals into specific end-members by decomposing the IRM acquisition curves (Heslop et al., 2002; Kruiver et al., 2001).

Early diagenetic processes are often described as steady state diagenesis, where fluxes of oxidants and reductants are balanced, and thus, redox fronts are located at specific depths relative to the sediment surface over long periods (Berner, 1981; Froelich et al., 1979). However, marine sediments are usually subject to non-steady state diagenesis, triggered by changes in fluxes of electron donors and acceptors and/or depositional conditions including sedimentation and carbon burial rates (e.g., Kasten et al., 2003; Pruyssers et al., 1993). Non-steady state conditions typically cause vertical shifts of redox boundaries and geochemical reaction fronts and the dissolution of primary and formation of secondary mineral phases. Typical examples of such diagenetic mineral precipitation are the formation of Fe sulfides (e.g., Kasten et al., 1998; März et al., 2008; Passier et al., 1996; Riedinger et al., 2005) and barite (e.g., Arndt et al., 2006; Henkel et al., 2012; Riedinger et al., 2006). Consequently, there is often a considerable age offset between the time when an authigenic mineral precipitates or other secondary signals form and the age of the surrounding host sediment. Since sedimentary proxies including biogenic barite and magnetic susceptibility have been intensively used for paleoclimatic and oceanographic reconstructions or as a correlation tool (e.g., Dymond et al., 1992; Thompson et al., 1980), the diagenetic alteration of the initially deposited material needs to be considered to avoid misinterpretation of the sedimentary record. Non-steady state diagenesis does not only occur on timescales from centuries to several thousands of years (e.g., Kasten et al., 1998; Riedinger et al., 2005), but can also affect biogeochemical and diagenetic processes on geological timescales (>millions of years) by changes in geochemical and depositional conditions (e.g., Meister, 2015). Deeply buried Cretaceous shales in sediments from the Demerara Rise in the equatorial Atlantic, for example, stimulate biogeochemical

processes in the overlying sediment column even 100 Ma after their deposition (Arndt et al., 2006). Present-day pore-water and solid-phase signatures in sediments at the Bowers Ridge in the Bering Sea (IODP Expedition 323 Site U1341) reflect the impact of changes in the deposition and reactivity of organic matter that occurred ~2.5 Ma ago (Wehrmann et al., 2013). In addition to variations in organic matter quantity and reactivity related to oceanographic and climatic changes, changes in biogeochemical processes can also be induced by tectonic dynamics including fluid flow along faults, hydrothermal circulation and frictional heating (e.g., Fischer et al., 2013; Wehrmann & Riedinger, 2016). For example, recalcitrant organic matter in subseafloor sediments from the Nankai accretionary prism might be reactivated caused by frictional heating associated with earthquakes or advective fluid flow (Ijiri et al., 2018; Riedinger et al., 2015). Marine sediments represent one of the most valuable archives to reconstruct changes in paleoceanographic, depositional and climatic conditions over Earth's history. In order to interpret this record reliably, it is crucial to consider and assess the impact of ocean floor migration on post-depositional overprint of the primary sediment composition.

International Ocean Discovery Program (IODP) Expedition 370 (Temperature Limit of the Deep Biosphere off Muroto) established Site C0023 down to 1,180 m below seafloor (mbsf) in the Nankai Trough off Cape Muroto, Japan, to explore the upper temperature limit of microbial life in marine sediments (Heuer et al., 2017a). Site C0023 has experienced a significant increase in sedimentation rates associated with the migration over vast distances from its initial position in the central Shikoku Basin to the Nankai Trough caused by the Philippine Sea plate motion (Hagino & the Expedition 370 Scientists, 2018; Mahony et al., 2011). With ongoing burial, the temperature rapidly rose across the sediment column, leading to a present-day temperature gradient of  $110^{\circ}\text{C km}^{-1}$  (Heuer et al., 2020). While the impact of the Philippine Sea plate migration on variations in the sediment composition has been extensively investigated (e.g., Saitoh et al., 2015; Underwood & Steurer, 2003), the effect of a tectonically induced migration of ocean floor through different depositional regimes on the biogeochemical dynamics within the sediments in the Nankai-Shikoku-subduction system has not yet been studied.

In order to study long-term variations in biogeochemical and diagenetic processes as well as element fluxes at Site C0023, we combine a unique multi-disciplinary data set that includes shipboard high-resolution pore-water and gas data, organic carbon contents (Heuer et al., 2017a), and sedimentation rates and ages (Hagino & the Expedition 370 Scientists) with our solid-phase data comprising bulk sediment compositions, Fe speciation, and rock magnetic signals. One objective is to evaluate if reactive Fe is still available to serve as a potential energy substrate for microbially mediated processes in the deep and hot subseafloor sediments at Site C0023. In order to reliably quantify and characterize the different reactive Fe pools at Site C0023, we combine chemical sequential Fe extractions with IRM acquisition curve end-member unmixing and  $^{57}\text{Fe}$  Mössbauer spectroscopy analysis. We further reconstruct past variations in (bio-)geochemical and diagenetic processes driven by changing environmental conditions and assess how these changes affected the sedimentary Fe pool from its initial deposition to progressing burial and diagenetic alteration to the present-day situation. The succession of biogeochemical and diagenetic processes is merged into a conceptual geochemical process model.

## 2. Study Site

### 2.1. Geological Background

Site C0023 ( $32^{\circ}22.00'\text{N}$ ,  $134^{\circ}57.98'\text{E}$ ; 4,776 m water depth) is located in the Nankai Trough, 125 km southeast of Cape Muroto, Japan. The Nankai Trough represents an ideal area to explore the upper temperature limit of subseafloor life since it is characterized by high heat flows (Heuer et al., 2020; Yamano et al., 1992). Our study is integrated into a number of microbiological, geochemical, and sedimentological studies. This interdisciplinary approach offers an outstanding opportunity to investigate the prerequisites of deep microbial life. Site C0023 lies on the so-called Muroto Transect (Shipboard Science Party, 2001), which is perpendicular to the Nankai Trough (Heuer et al., 2017a). The Nankai Trough forms the subduction boundary between the southwest Japan arc (Eurasian plate) and the Shikoku Basin (Figure 1). The Shikoku Basin is part of the Philippine Sea plate that is subducting beneath the Eurasian plate at a current rate of 4–6  $\text{cm yr}^{-1}$  in a northwest direction (DeMets et al., 2010; Seno et al., 1993). The trench in general is relatively shallow with water depths <5,000 m below sea level (Shipboard Science Party, 1991). The subducting oceanic

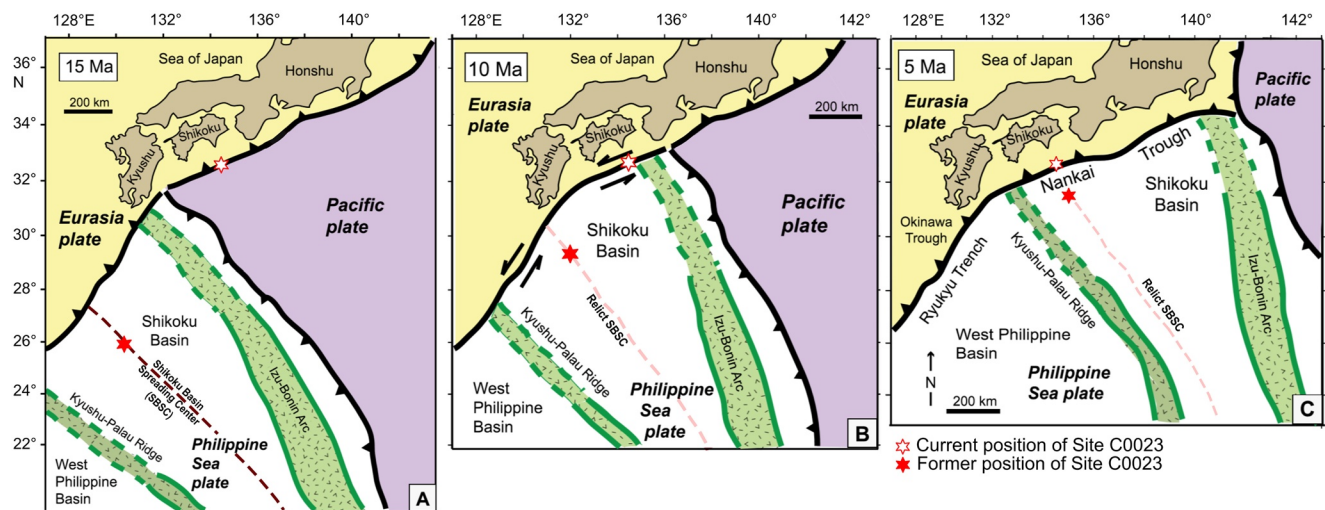


**Figure 1.** Simplified schematic plate tectonic reconstruction for the Shikoku Basin and the relative movement of Site C0023 over the past 15 Ma. Japan is held fixed at its current position. Opened and filled red stars represent the current position of Site C0023 and its position over the course of 15 Ma, respectively. Modified after Underwood & Guo (2018) (<https://creativecommons.org/licenses/by-nc/4.0/>).

lithosphere of the Shikoku Basin initially formed by rifting of the paleo-Izu-Bonin backarc and seafloor spreading in the eastern part of the Philippine Sea plate between 26 and 15 Ma. The Kyushu-Palau Ridge and the Shichito-Iwojima Ridge are relics of the former arc, which were separated by the spreading, limiting the Shikoku Basin to the east and west, respectively (Okino et al., 1994, 1999; Watts & Weissel, 1975). The Kinan Seamounts Chain runs along the axis of the basin and represents the relic of the extinct spreading center in the Shikoku Basin (e.g., Pickering et al., 2013).

Site C0023 has moved relative to its present-day geographic position due to motion of the Philippine Sea plate (e.g., Mahony et al., 2011). Figure 1 shows a schematic plate tectonic reconstruction for the Shikoku Basin and the relative movement of Site C0023 over the past 15 Ma. The oceanic basement of Site C0023 was formed ~16 Ma ago (Shipboard Science Party, 1991, 2001) during a phase when seafloor spreading in the Shikoku Basin ceased to be active (Chamot-Rooke et al., 1987; Okino et al., 1994). Mahony et al. (2011) reconstructed the tectonic evolution of the Philippine Sea plate relative to the Eurasian plate for the past 15 Ma. From 15 to 6 Ma, the triple junction between the Pacific plate, Philippine Sea plate and southwest Japan moved northward, resulting in the subduction of the Philippine Sea plate beneath Kyushu and Shikoku islands. Extensive volcanic activity began at 8 and 6 Ma on Kyushu and in SW Japan, respectively, and is related to the formation of a volcanic front and a deeply penetrating subducting slab (Kamata & Kodama, 1994). The Izu-Bonin arc started colliding with the Honshu arc during the late Miocene, generating the Izu-collision zone. The subduction of the Philippine Sea plate and off-scraping of the trench wedge sediment from the descending Philippine Sea plate led to the formation of the Nankai accretionary prism (Costa Pisani et al., 2005; Le Pichon et al., 1987; Taira et al., 1992). Site C0023 is located at the seaward-end of this accretionary prism (Heuer et al., 2017a).

## 2.2. Sedimentary Setting

The incoming sedimentary sequence of the Nankai subduction zone at Site C0023 is ~1.2 km thick and four lithological units are differentiated (Table 1; Figure S1). In general, a ~500 m thick layer of turbidite-deposited mud, silt, and sand (Unit II) accumulated on a ~620 m thick sequence of basin style-deposited hemipelagic mudstones intercalated with tuffs (Unit III and IV). The decollement zone is located between 760 and 800 mbsf.

The Trench-wedge facies (Unit II), Pleistocene in age, is divided into three subunits. The Axial trench-wedge facies (Subunit IIA) mainly consists of thick sand and silt intervals in hemipelagic mud, whereas the Outer trench-wedge facies (Subunit IIB) contains more mud and less sand and silt. The sand- and silt-rich



**Table 1**  
*Lithological Units and Associated Facies, Lithology, Depth, Age, and Sedimentation Rates of Site C0023 (Heuer et al., 2017b)*

Unit	Facies	Lithology	Depth (mbsf)	Age (Ma)	Sedimentation rate (cm kyr <sup>-1</sup> )
IIA	Axial trench-wedge	Hemipelagic and pelagic sand, muddy sand, turbidite-deposited silt and sandstones	189–318.5		
IIB	Outer trench-wedge	Hemipelagic and pelagic mud, turbidite-deposited mudstones	353–428	0.29	131.9
IIC	Trench-to-basin transition	Turbidite-deposited silt and sand, tuffs and volcanoclastic sediments	428–494	0.29–0.43	61.0
III	Upper Shikoku Basin	Heavily bioturbated volcanoclastic mudstones	494–637.5	0.43–2.53	9.3–6.0
IV	Lower Shikoku Basin	Heavily bioturbated mudstones with green ash-rich laminae	637.5–1112	2.53–13.53	6.0–3.5
V	Acidic volcanoclastics	Mudstones and felsic ash	1112–1125.9		
	Basaltic basement	Hyaloclastites	1125.9		

*Note.* Ages and sedimentation rates are based on biostratigraphic studies on calcareous nannofossil assemblages (Hagino & the Expedition 370 Scientists, 2018).

intervals are related to rapid transportation of shelf sand and mud during high-density turbidity flows. The Trench-to-basin transitional facies (Subunit IIC) comprises volcanoclastic beds with high contents of vitric ash (<75%) and igneous crystals, that are mixed into the overlying mudstones by bioturbation. The Upper Shikoku Basin facies (Unit III) is Pleistocene to Pliocene in age and characterized by bioturbated mudstones with 4–10 cm thick volcanoclastic sand-rich beds and calcareous burrows. The Lower Shikoku Basin facies (Unit IV) was deposited during Miocene times. It is dominated by greenish, heavily bioturbated mudstones and ash-rich laminae with high smectite and detrital chlorite contents. The extent of bioturbation and presence of burrows increase from Unit II to Unit IV, as evidenced by a higher occurrence of calcareous burrows in the Lower Shikoku Basin facies (Heuer et al., 2017a; Taira & Ashi, 1993). The mudstones in Unit IV are intensively altered by low-temperature hydrothermal fluid flow (Figure S1; e.g., Tsang et al., 2020). Pale-yellow to pinkish alteration patches and burrow infills of rhodochrosite (MnCO<sub>3</sub>) as well as strata-bound and vein-filling crystals of barite (BaSO<sub>4</sub>) could be observed in the lower parts of Unit IV. In addition, multiple intervals of green-colored mineralization associated with altered smectite and chlorite are found in the Lower Shikoku Basin facies. Unit V represents the oldest lithological unit at Site C0023. This 14 m thick greenish layer consists of acidic volcanoclastics with a high abundance of chlorite and smectite. Hyaloclastite deposits with glass and basalts as the dominant clasts characterize the lithologic basement (Heuer et al., 2017a; Taira & Ashi, 1993).

The total clay mineral abundance, inferred from shipboard X-ray diffraction (XRD) analyses, moderately increases with depth from 50% in Subunit IIA to 75% in Unit IV. In contrast, quartz and plagioclase contents are enriched (25%) in Subunits IIA and IIB, which is related to the presence of sand- and silt-rich intervals. As a result, porosity values generally decrease from 40% to 50% in Subunit IIA to 32% at the base of Unit IV. Calcium carbonate (CaCO<sub>3</sub>) contents are generally low (average of ~3.4 wt%), with high scatter from Subunit IIC to Unit IV and contents up to 21.6 wt% due to the occurrence of calcareous horizons (calcite-cemented mudstones) and carbonate-rich hydrothermal alteration patches. A more detailed lithology description of each lithological unit can be found in Heuer et al. (2017a).

The transition from basin style-deposited hemipelagic mudstones to turbidite-deposited mud, silt, and sand led to a significant increase in sedimentation rates from 6.0 to 3.5 cm kyr<sup>-1</sup> during late Miocene and Pliocene times in Unit IV to 131.9 cm kyr<sup>-1</sup> in the middle Pleistocene in Subunit IIB (Table 1; Hagino & the Expedition 370 Scientists, 2018).

At present, the temperature at Site C0023 increases from ~1.6°C at the sediment-water interface up to 120 ± 3°C in the deepest core retrieved from the basement at 1177 mbsf, leading to an in situ temperature gradient of 110°C km<sup>-1</sup> (Heuer et al., 2020). The current heat flow is 140 mW m<sup>-2</sup> (Heuer et al., 2017a). Based on basin modeling approaches, the temperature and burial history were reconstructed at different sites along the Muroto Transect (Horsfield et al., 2006; Tsang et al., 2020). Consistently, best fits with measured temperature and heat flow data were reached with a basin modeling scenario, in which high heat flows close to the spreading center of the 15 Ma-old oceanic lithosphere are followed by a transition to lower

off-axis heat flows and a short increase up to  $180 \text{ mW m}^{-2}$  around 2 Ma associated with increased volcanic activity in the Japanese Island arc. In addition to heating associated with ongoing burial, evidence for short-term (<3 days) and localized heating caused by low-temperature hydrothermal fluids ranging from  $\sim 120^\circ\text{C}$  to  $220^\circ\text{C}$  within fracture zones has been found at Site C0023. As a result, hydrothermal mineralization assemblages including veins and stratabound alteration patches rich in  $\text{BaSO}_4$  and  $\text{MnCO}_3$  are formed (Tsang et al., 2020).

### 3. Material and Methods

#### 3.1. Shipboard Sampling and Pore-Water and Gas Analyses

During IODP Expedition 370, a total of 112 sediment cores were collected from Hole C0023A, covering a depth range from 189 to 1,180 mbsf (Heuer et al., 2017a). All sediment depths used in this study are reported as corrected core depths below seafloor (CSF-B). Whole-round core (WRC) samples for geochemical analyses were selected based on X-ray computed tomography (CT) image analysis to avoid horizons with fractures and disturbances and taken immediately after dividing the core into sections. The WRC samples varied in length between 10 and 80 cm. Pore-water was extracted from WRC samples using a titanium squeezer modified after the stainless-steel squeezer of Manheim and Sayles (1974). The WRCs dedicated to pore-fluid sampling were transferred into an  $\text{N}_2$ -flooded glovebag in which they were removed from the liner. To minimize seawater and drilling fluid contamination, the outer sediment layer (3–7 mm) was removed prior to squeezing. The samples were transferred into the titanium vessels and subsequently squeezed at 30,000 lb. Some samples from the deeper core had to be squeezed at 60,000 lb to increase the total pore-water volume yield. Chlorinity titrations were performed on water extracted at both forces to assess whether higher pressures caused sample freshening. The collected pore water was filtered through a Millipore Millex-LH hydrophilic  $0.45 \mu\text{m}$  polytetrafluoroethylene (PTFE) disposable filter (Heuer et al., 2020; Morono et al., 2017). The whole-round squeeze cakes remaining after pore-water extraction were transferred into gas-tight aluminum bags, flushed with  $\text{N}_2$ , and subsequently vacuum-sealed. Vacuum-sealed bags were stored at  $-20^\circ\text{C}$  for solid-phase analyses conducted in this study. Further details on the onboard sampling are given in the Method Chapter of the Expedition Report (Morono et al., 2017).

Pore-water and dissolved gas analyses were carried out onboard D/V *Chikyu* as described in Morono et al. (2017). In brief, sulfate concentrations were determined using a Dionex ICS-2100 ion chromatograph with an uncertainty of 0.02 mM. Pore-water samples with seawater contamination >4% were excluded (Heuer et al., 2017a). Methane concentrations were analyzed with an Agilent 7890B gas chromatograph equipped with a packed column (HP PLOT-Q) and flame ionization detector (FID).

Dissolved Fe and hydrogen sulfide measurements were conducted with a Hach DR 2800 spectrophotometer. Dissolved Fe concentrations were determined using the ferrozine method after Stookey (1970). The detection and quantification limits for diluted samples were 0.3 and  $0.8 \mu\text{M}$ , respectively. Hydrogen sulfide measurements were performed following the methylene blue method after Cline (1969), whereby detection and quantification limits were 0.2 and  $0.4 \mu\text{M}$ , respectively.

Dissolved inorganic carbon (DIC) was measured with a Marianda automated infrared inorganic carbon analyzer (AIRICA) system with an uncertainty of 0.052 mM. The shipboard pore-water and gas data are reported in Tables 14 and 22 of the Expedition Report, respectively (Heuer et al., 2017a).

#### 3.2. Inorganic Solid-Phase Analyses

##### 3.2.1. Bulk Sediment Composition

Inorganic solid-phase analyses were conducted in the laboratory at the Alfred Wegener Institute (AWI) Helmholtz Centre for Polar and Marine Research in Bremerhaven, Germany. Sub-samples from squeeze cakes were freeze-dried and ground in an agate ball mill for subsequent solid-phase analyses. In this way, the sub-samples were homogenized and integrated over the whole length of the WRC samples. For analyses of the bulk sediment composition,  $\sim 50 \text{ mg}$  of homogenized sediment was fully dissolved in a mixture of 65%  $\text{HNO}_3$  (3 mL), 30%  $\text{HCl}$  (2 mL) and 40% suprapur<sup>®</sup> HF (0.5 mL).  $\text{HNO}_3$  and  $\text{HCl}$  were of sub-boiling distilled quality. The total acid digestions were performed in a CEM Mars Xpress microwave system according

to the procedure described by Nöthen and Kasten (2011). This method yields data for total Fe ( $Fe_{total}$ ), S ( $S_{total}$ ), and Al ( $Al_{total}$ ) contents. Standard reference material (NIST SRM 2702) and blanks were processed with each set of samples. Elemental concentrations were determined by inductively coupled plasma optical emission spectrometry (ICP-OES) analysis (iCAP 7400, Thermo Fisher Scientific Inc.) under application of an internal yttrium standard. The recoveries for the NIST SRM 2702 were  $97.1 \pm 4.0\%$  for  $Al_{total}$ ,  $94.7 \pm 3.4\%$  for  $Fe_{total}$  and  $101.0 \pm 3.7\%$  for  $S_{total}$  ( $n = 15$ ). Duplicate samples were analyzed to ensure that the elemental contents are representative for the whole WRC interval. The relative differences between duplicate samples were  $<5\%$  (Table S1).

### 3.2.2. Acid Volatile Sulfide and Chromium Reducible Sulfur

Acid volatile sulfide (AVS) and chromium reducible sulfur (CRS) were determined gravimetrically on  $\sim 1$  g of homogenized sediment by a two-step extraction. AVS includes Fe monosulfides whereas CRS is considered to represent pyrite. AVS was extracted with boiling 6 M HCl (Cornwell & Morse, 1987) and CRS using a  $CrCl_2$  solution (e.g., Canfield et al., 1986; Zhabina & Volkov, 1978). Sulfide that is released during both extraction steps was trapped as  $Ag_2S$ . The amounts of Fe bound to AVS and CRS were calculated from extracted sulfur using the stoichiometry 1:1 (FeS) and 1:2 (FeS<sub>2</sub>), respectively. Analytical precision was determined using an in-house sediment standard (HE443-077-cc; anoxic sediment from the North Sea) and a non-reference pyrite standard ( $>90\%$  pure; hydrothermal origin). Repetitive analyses resulted in FeS and pyrite contents of  $0.02 \pm 0.01$  wt% ( $n = 8$ ) and  $0.88 \pm 0.07$  wt% ( $n = 9$ ), respectively, for the in-house standard and pyrite contents of  $86.28 \pm 4.35$  wt% ( $n = 9$ ) for the pyrite standard.

### 3.2.3. Sequential Extraction of Fe (Oxyhydr)Oxides

Sequential extractions following the protocols described by Poulton and Canfield (2005) and Henkel et al. (2016) were applied on  $\sim 50$  mg of freeze-dried and homogenized sediment (Table S2). It typically targets four Fe pools, namely (a) Fe bound in carbonates ( $Fe_{carb}$ ), (b) easily reducible Fe oxides (ferrihydrite and lepidocrocite;  $Fe_{ox1}$ ), (c) reducible Fe oxides (goethite and hematite;  $Fe_{ox2}$ ) and (d) magnetite ( $Fe_{mag}$ ). However, in order to emphasize the operational nature of sequential extraction, an extraction stage-based labeling of fractions ( $Fe_{aca}$ ,  $Fe_{hyam}$ ,  $Fe_{di-ct}$ ,  $Fe_{oxa}$  after Henkel et al., 2016) rather than the conventional terminology is used in this study (Table S2). The sum of all sequentially leached Fe pools is defined as “reactive” Fe, which refers to the reactivity towards hydrogen sulfide (Poulton et al., 2004). “Microbial reducible” Fe(III), however, conventionally only comprises Fe bound in carbonates and easily reducible Fe oxides (e.g., Laufer et al., 2020). All extraction steps were carried out under  $N_2$ -atmosphere at room temperature. The sediment samples were first treated with 5 mL of 1 M  $MgCl_2$  (pH 7) for 2 h in order to extract pore-water constituents and adsorbed Fe (Heron et al., 1994; Tessier et al., 1979). The sediment-extraction reagent-suspensions were shaken on a vertical rotating shaker for the respective times and subsequently centrifuged at 4,000 rpm for 5 min. The supernatant was filtered through a 0.2  $\mu m$  polyethersulfone membrane. Splits of all extracts were analyzed by ICP-OES after dilution in 0.3 M  $HNO_3$  or ultrapure water (in case of Na-dithionite as extractant) for the determination of extracted Fe, Al, and Si. Standards were adapted to the different extraction matrices and all data were corrected for effects of different ionic strengths by use of an internal yttrium standard. Based on triplicate measurement of each sample, the relative standard deviation was  $<2\%$ . The in-house standard HE443-077-cc with overall comparable Fe contents to the C0023 samples resulted in values of  $4.43 \pm 0.10$  wt% for  $Fe_{aca}$ ,  $3.38 \pm 0.08$  wt% for  $Fe_{hyam}$ ,  $2.78 \pm 0.10$  wt% for  $Fe_{di-ct}$  and  $1.04 \pm 0.03$  wt% for  $Fe_{oxa}$  ( $n = 8$ ). These values were in the range of respective Fe contents determined over the course of 5 years in the laboratories at the AWI ( $Fe_{aca} = 4.57 \pm 0.21$  wt%;  $Fe_{hyam} = 3.15 \pm 0.25$  wt%;  $Fe_{di-ct} = 2.61 \pm 0.22$  wt%;  $Fe_{oxa} = 1.07 \pm 0.10$  wt%;  $n = 26$ ). The relative differences between duplicate samples are listed in Table S3.

### 3.3. Total Organic Carbon and Algal Biomarkers

Total organic carbon (TOC) and nitrogen (TN) analyses were conducted onboard D/V *Chikyū* using a Thermo Finnigan Flash EA 1112 CHNS analyzer. TOC contents were determined by subtraction of inorganic carbon (IC; Coulometrics 5012  $CO_2$  coulometer) from total carbon contents (TC). The TOC/N ratio was determined as a source indicator of the organic matter (Morono et al., 2017). TOC and TN data are reported in Table 20 of the Expedition Report (Heuer et al., 2017a).

The stable carbon isotopic composition of TOC ( $\delta^{13}\text{C}$ -TOC) and biomarker analyses were performed in the laboratory at the MARUM—Center for Environmental Sciences, University of Bremen, Germany. Prior to  $\delta^{13}\text{C}$ -TOC analysis, ground and homogenized samples were treated with 12.5% HCl to remove inorganic carbon and oven-dried. Analysis was performed with a Thermo Scientific Flash 2000 elemental analyzer coupled to a Thermo Delta V Plus IRMS. The  $\delta^{13}\text{C}$ -TOC values are expressed relative to VPDB (Vienna Pee Dee Belemnite). For biomarker analyses, samples were extracted using a modified Bligh and Dyer extraction technique as described in Sturt et al. (2004). After extracting twice with methanol (MeOH):dichloromethane (DCM):phosphate buffer (2:1:0.8, v/v/v) and twice with MeOH:DCM:TCA buffer (2:1:0.8, v/v/v), a fifth extraction step was added using dichloromethane:methanol (3:1, v/v). An aliquot of the dried lipid extract was measured on a Bruker maXis Plus ultra-high-resolution quadrupole time-of-flight mass spectrometer (Q-TOF) coupled with an APCI II ion source to Dionex Ultimate 3000RS ultra-high-pressure liquid chromatography (UHPLC). Coccolithophore (alkenones) and eustigmatophyte (long-chain diols) biomarkers were separated using two coupled Acquity BEH amide columns ( $2.1 \times 150$  mm,  $1.7 \mu\text{m}$ ; Waters, Eschborn, Germany) following protocols described in Becker et al. (2015).

### 3.4. IRM Acquisition Curves and End-Member Unmixing

All magnetic measurements were performed in the paleomagnetic laboratory at the Center for Advanced Marine Core Research, Kochi University, Japan. IRM acquisition curves were measured on 46 samples at room temperature using a Princeton Measurements Corporation Vibrating Sample Magnetometer to characterize the magnetic mineral assemblages. Samples were dry and powdered sediment filled into gelatin capsules and packed with cotton wool ( $\sim 600$  mg). IRM was imparted stepwise (non-linearly) up to a maximum field of 1 T, with an average time of 200 ms. 100 data points describe one IRM acquisition curve. The IRM acquisition curves for a magnetic mineral assemblage can be approximated by cumulative log-Gaussian functions using three parameters: the estimated saturation IRM, the mean coercivity ( $B_h$ ) of a magnetic phase (i.e., the field at which half of the total IRM is reached on a logarithmic field scale), and the dispersion parameter (DP), which describes the width of the coercivity distribution of a mineral phase (given by one standard deviation in log space; Kruiver et al., 2001; Maxbauer et al., 2016; Robertson & France, 1994). All IRM acquisition curves were unmixed using the web application MAX UnMix by Maxbauer et al. (2016).

### 3.5. Magnetic Susceptibility

The magnetic susceptibility is defined as the ratio between the induced magnetization of a material to an applied magnetic field. It is used as a relative proxy indicator for changes in the sedimentary composition and as a proxy for magnetic mineral concentration. Low-field and low-frequency (0.465 kHz) magnetic susceptibility ( $\chi_{\text{lf}}$ ) was measured on 223 discrete samples (7 cc plastic cubes) using an MS2 Bartington apparatus.

### 3.6. $^{57}\text{Fe}$ Mössbauer Spectroscopy

To improve the interpretation of sequential extraction data,  $^{57}\text{Fe}$  Mössbauer spectroscopy analysis was performed on three representative samples (370-C0023A-18R-1, 19.0–41.0 cm; 370-C0023A-81R-7, 0.0–30.0 cm; 370-C0023A-105R-2, 0.0–45.0 cm) from different depths (430, 850, and 1,080 mbsf, respectively) at the Center for Applied Geosciences at the University of Tübingen, Germany. Freeze-dried and mortared sediment samples were loaded into Plexiglas holders (area  $1 \text{ cm}^2$ ), forming a thin disc. Samples were then loaded to the instrument and spectra were collected at room temperature (295 K), 77 K, and 5 K using a constant acceleration drive system (WissEL) in transmission mode with a  $^{57}\text{Co}/\text{Rh}$  source. All spectra were calibrated against a  $7 \mu\text{m}$  thick  $\alpha$ - $^{57}\text{Fe}$  foil that was measured at room temperature. Analysis was carried out using Recoil (University of Ottawa). Based on the prevalent dominance of Fe-rich, clay-sized phyllosilicates (Heuer et al., 2017a), the Lorentzian Site Analysis routine was performed to produce consistent fits and serviceable results that allowed the investigation of Fe(II)/(III) ratios and the comparison with a reference data base (Murad, 1998, 2010).



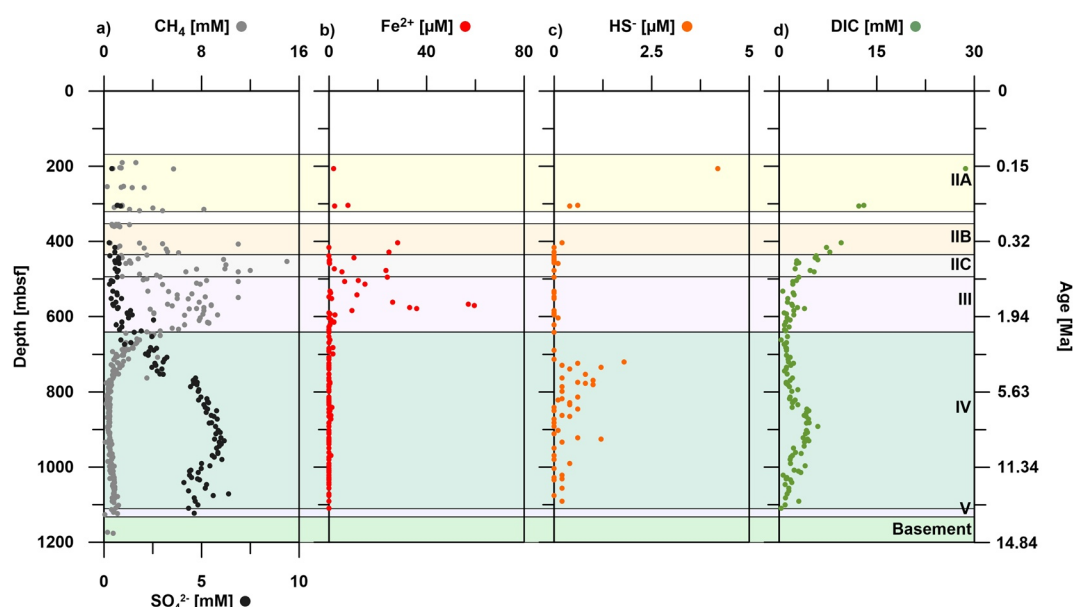


**Figure 2.** Pore-water profiles of (a) sulfate ( $\text{SO}_4^{2-}$ ), methane ( $\text{CH}_4$ ), (b) dissolved Fe ( $\text{Fe}^{2+}$ ), (c) hydrogen sulfide ( $\text{HS}^-$ ), and (d) dissolved inorganic carbon (DIC) at Site C0023 from Heuer et al. (2017a). Lithological units (Heuer et al., 2017a) are indicated on the right. Corresponding ages on the right-side y-axis are based on the age model by Hagino & the Expedition 370 Scientists (2018).

## 4. Results

### 4.1. Pore-Water and Gas Geochemistry

Pore-water sulfate ( $\text{SO}_4^{2-}$ ) concentrations range from 0.3 to 0.9 mM between 206.5 (shallowest sample) and 550 mbsf (Figure 2a). Below 550 mbsf, sulfate concentrations gently increase to 3 mM at 750 mbsf, followed by a strong increase of up to 6.2 mM at 930 mbsf. Sulfate concentrations decrease between 950 and 1,050 mbsf by 1.5 mM and scatter between 5 and 7 mM towards the sediment-basement interface. Some scatter in sulfate concentrations can be attributed to contamination with seawater-derived sulfate, as described in the Expedition Report (Heuer et al., 2017a).

Methane ( $\text{CH}_4$ ) concentrations strongly fluctuate between 190 and 750 mbsf, varying from 0.3 to ~15 mM (Figure 2a). The highest values are detected between 410 and 640 mbsf. Below,  $\text{CH}_4$  concentrations decrease to <0.5 mM at 770 mbsf and remain low down to 900 mbsf, before increasing again to maximum values of 1.2 mM at a depth of 1,100 mbsf. Dissolved Fe ( $\text{Fe}^{2+}$ ) was observed between 200 and 600 mbsf with a maximum concentration of 60  $\mu\text{M}$  at 570 mbsf (Figure 2b).  $\text{Fe}^{2+}$  concentrations decrease and remain close or below quantification limits of 0.8  $\mu\text{M}$  below 600 mbsf. Dissolved hydrogen sulfide ( $\text{HS}^-$ ) concentrations are generally low at Site C0023. The shallowest sample at ~200 mbsf shows the highest values of 4.2  $\mu\text{M}$  (Figure 2c). The hydrogen sulfide concentrations are close to or below detection limit of 0.2  $\mu\text{M}$  between 300 and 720 mbsf, followed by an interval with concentrations of up to 1.8  $\mu\text{M}$  down to the bottom of the core. Dissolved inorganic carbon (DIC) values decrease from ~30.0 to 2 mM between 200 and 600 mbsf and remain <2 mM further downcore (Figure 2d).

### 4.2. Inorganic Sediment Geochemistry

$\text{Fe}_{\text{total}}$  contents range from 3.4 to 5.1 wt% with an average value of 4.2 wt% (Figure 3a). The  $\text{Fe}_{\text{total}}/\text{Al}_{\text{total}}$  profile generally mimics the  $\text{Fe}_{\text{total}}$  profile within the range of 0.43–0.61 (Figure 3b), and thus, close to an average shale value of 0.55 (Turekian & Wedepohl, 1961). Both,  $\text{Fe}_{\text{total}}$  and  $\text{Fe}_{\text{total}}/\text{Al}_{\text{total}}$  display highest values of 5.1 wt% and 0.61, respectively, at the lower end of Unit IV at ~1,100 mbsf.

$\text{S}_{\text{total}}$  contents show strong variability between 0.04 and 0.61 wt% with an average value of 0.20 wt% (Figure 3c). Intervals with elevated values occur between 500 and 600 mbsf, 640 and 770 mbsf as well as 900 and

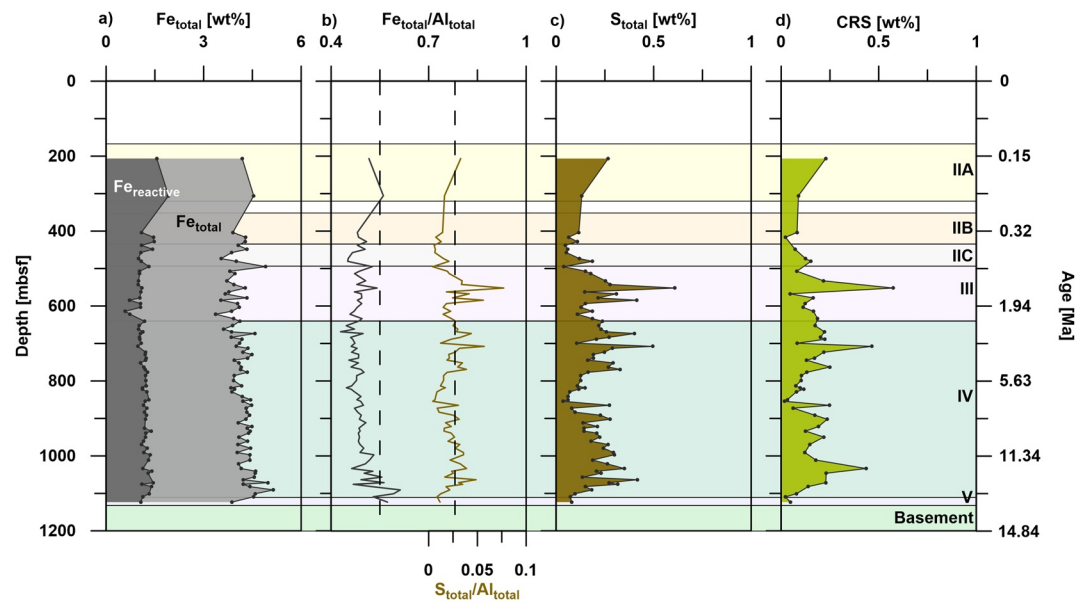


**Figure 3.** Down-core solid-phase profiles of (a) reactive Fe ( $Fe_{\text{reactive}} = Fe_{\text{aca}} + Fe_{\text{hyam}} + Fe_{\text{di-ct}} + Fe_{\text{oxa}}$ ; see Figure 4), total Fe ( $Fe_{\text{total}}$ ), (b)  $Fe_{\text{total}}/Al_{\text{total}}$ ,  $S_{\text{total}}/Al_{\text{total}}$ , (c) total S ( $S_{\text{total}}$ ), and (d) chromium reducible sulfur (pyrite). Dashed vertical lines indicate average shale content (Turekian & Wedepohl, 1961). Color shading and corresponding ages as in Figure 2.

1,100 mbsf. The  $S_{\text{total}}/Al_{\text{total}}$  profile resembles the  $S_{\text{total}}$  profile (Figure 3b). The ratio varies over depth with an average value 0.02, and thus, is close to average shale with 0.03 (Turekian & Wedepohl, 1961). While AVS was absent, CRS contents fluctuate over depth between 0.02 and 0.57 wt% (Figure 3d) and mimic the  $S_{\text{total}}$  profile, suggesting that bulk S is mainly present as pyrite.

$Fe_{\text{reactive}}$ , here comprised of the sum of the sequentially extracted Fe, represents  $\sim 25\%$  of  $Fe_{\text{total}}$  (Figure 3a).  $Fe_{\text{aca}}$  is elevated up to 1 wt% in Subunits IIA and IIB and generally decreases with depth to 0.05 wt% (Figure 4a).  $Fe_{\text{hyam}}$  is the dominant reactive Fe fraction ( $\sim 60\%$  of  $Fe_{\text{reactive}}$ ) with contents up to 0.97 wt% and an

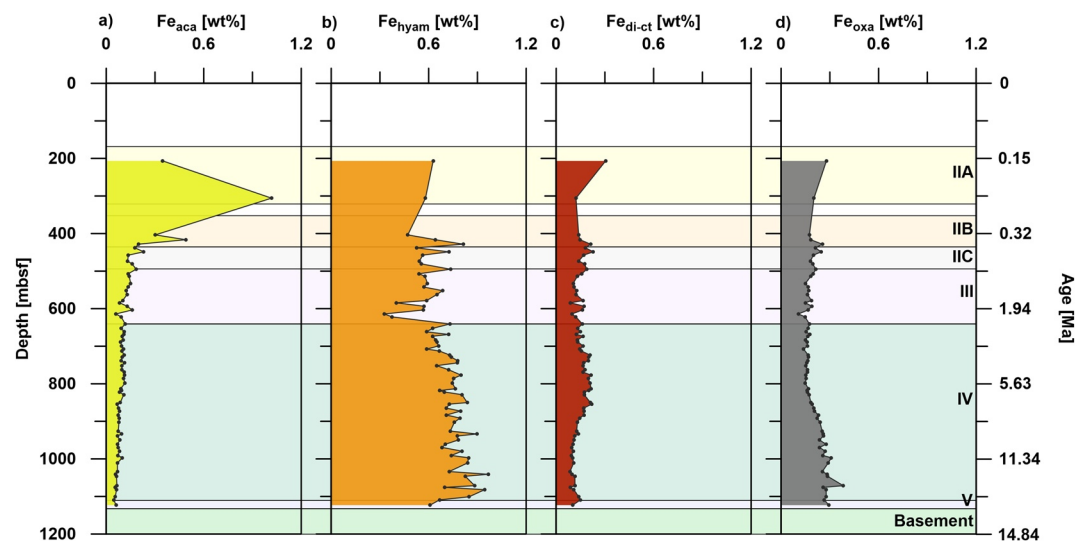


**Figure 4.** Down-core solid-phase profiles of sequentially extracted (a)  $Fe_{\text{aca}}$  (Na-acetate-leachable Fe), (b)  $Fe_{\text{hyam}}$  (Hydroxylamine-HCl-leachable Fe), (c)  $Fe_{\text{di-ct}}$  (Na-dithionite-leachable Fe), and (d)  $Fe_{\text{oxa}}$  ( $NH_4$ -oxalate/oxalic acid-leachable Fe). Color shading and corresponding ages as in Figure 2. Note that there are only three data points between 200 and 400 mbsf.

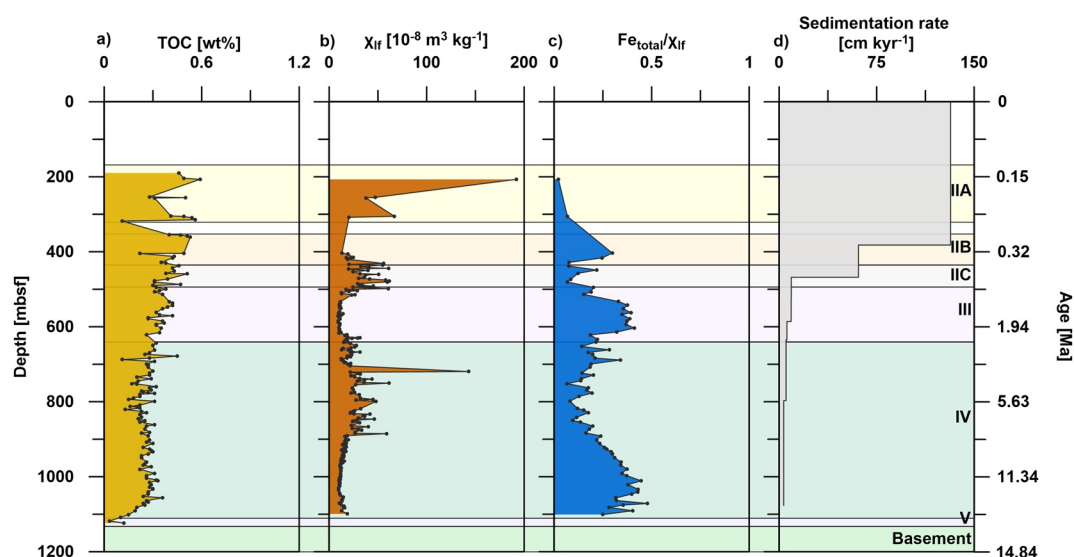


**Figure 5.** Down-core solid-phase profiles of (a) total organic carbon (modified from Heuer et al., 2017a), (b) magnetic susceptibility  $\chi_{ir}$ , (c)  $Fe_{total}/\chi_{ir}$ , which indicates the intensity of magnetite dissolution (Funk et al., 2004), and (d) sedimentation rates (from Hagino & the Expedition 370 Scientists, 2018). Color shading and corresponding ages as in Figure 2.

overall increasing trend with depth (Figure 4b). The average contents of  $Fe_{di-ct}$  and  $Fe_{oxa}$  are 0.15 and 0.20 wt%, respectively (Figures 4c and 4d). The  $Fe_{di-ct}$  and  $Fe_{oxa}$  profiles both display an overall decrease in Unit II and III. While  $Fe_{di-ct}$  contents are elevated with up to 0.22 wt% between 720 and 890 mbsf and decrease further below,  $Fe_{oxa}$  shows the opposite trend with lower contents in the top of Unit IV and increased values (0.27 wt% on average) between 890 mbsf and the bottom of Unit IV.

### 4.3. Total Organic Carbon and Algal Biomarkers

While TOC generally decrease downcore from 0.6 wt% in Unit II to 0.3 wt% in the lower interval of Unit III, the contents are relatively constant at around 0.25 wt% in Unit IV (Figure 5a). TOC/N ratios steadily decrease from 12 in Subunit IIA to <4 at the bottom of Unit IV and are generally proportional to the TOC contents (Figure S2a; Heuer et al., 2017a). The  $\delta^{13}C$ -TOC values gradually increase from  $-26\text{‰}$  in the upper part of Unit II up to  $-21\text{‰}$  in Unit III. Below 600 mbsf,  $\delta^{13}C$ -TOC values slightly shift towards lighter values towards the bottom of Unit IV with values ranging between  $-24\text{‰}$  and  $-22\text{‰}$  (Figure S2b).

Two types of algal lipid biomarkers are detected in the employed analytical window: long-chain diols, which are suggested to be sourced from eustigmatophyte algae (Volkman et al., 1992), and long-chain alkenones and alkyl alkenoates, which are diagnostic biomarkers for coccolithophores (Brassell et al., 1986). Due to the lack of representative standards we are not reporting absolute concentrations but instead report the integrated peak area of the sum of all detected diols normalized to kg extracted sediment (PA/kg) for each depth (Figure S2c and S2d). Long-chain diols are only detected in Unit IIA through Unit III. In this interval  $C_{26}$  to  $C_{34}$  diols are observed, with  $C_{30:0}$  1,15 diols and  $C_{32:0}$  diols being most abundant. Summed long-chain diol abundance ranges from 221 to 32,000 PA/kg with a maximum observed at 350 mbsf. Diols are not detected below 620 mbsf. Long-chain alkenones are present from the top of the core down to 860 mbsf.  $C_{37}$ ,  $C_{38}$ , and  $C_{39}$  long-chain alkenones are most abundant, followed by  $C_{36}$  alkyl alkenoates. Similar to the long-chain diols, highest abundances of the summed alkenones and alkyl alkenoates are observed between 350 and 520 mbsf, with concentrations up to 300,000 PA/kg at the top of Unit III.

### 4.4. IRM End-Member Unmixing

After unmixing IRM acquisition curves of the studied samples, the magnetic mineral assemblages can be described by one to four coercivity end-members (EM) and by their contribution (extrapolated contribution

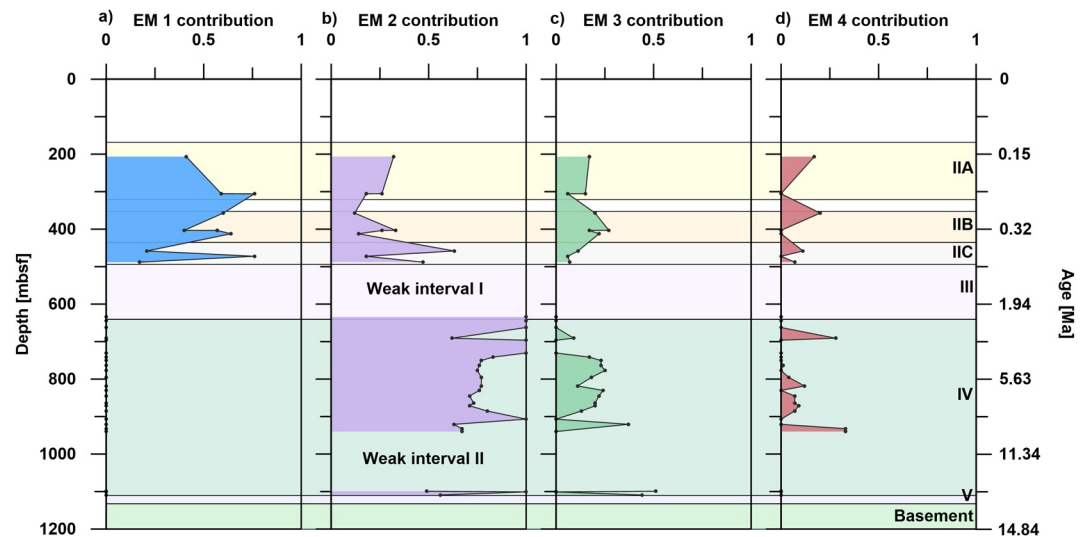


**Figure 6.** End-member plot showing the relative contributions to the total isothermal remanent magnetization of each end-member (EM) (a) greigite, (b) fine-grained magnetite, (c) hematite, and (d) coarse-grained magnetite in representative samples over depth obtained by using the MAX UnMix web application (Maxbauer et al., 2016). The coercivity distribution could not be modeled in two depth intervals due to low magnetic intensities, referred as to Weak interval I and II. Note that EM 1 is only identified between 200 and 500 mbsf. Color shading and corresponding ages as in Figure 2.

[EC]) to the total IRM (Maxbauer et al., 2016). The coercivity distributions of three representative samples (370-C0023A-3F-3, 80.0–105.0 cm, 370-C0023A-21R-2, 101.0–103.0 cm, and 370-C0023A-83R-2, 56.0–58.0 cm) at 206.5, 458.2, and 863.6 mbsf, respectively, are shown in Figure S3. EM 1 (blue) is an intermediate coercivity component with  $B_h$  of  $1.91 \log_{10}$  ( $\sim 81.3$  mT) and a narrow DP of  $\sim 0.15$ , which is interpreted as greigite (e.g., Roberts et al., 2011; Shi et al., 2017).  $B_h$  of EM 2 (purple) is  $1.61 \log_{10}$  ( $\sim 40.7$  mT), which is indicative of fine-grained magnetite (e.g., Abrajevitch et al., 2009). EM 3 (green) represents a higher coercivity component with  $B_h > 2 \log_{10}$  ( $> 100$  mT) and a wide DP (1.03), such as hematite (e.g., Abrajevitch & Kodama, 2011; Abrajevitch et al., 2009). EM 4 (red) is interpreted as coarse-grained magnetite with  $B_h$  of  $\sim 1.36 \log_{10}$  ( $\sim 22.9$  mT) and DP of 0.62.

Down-core variations in the relative proportion of each modeled EM are shown in Figure 6. Due to low magnetic minerals contents and consequently weaker magnetization in samples between 500 and 650 mbsf as well as 950 and 1,100 mbsf, these intervals are indicated as weak intervals I and II. EM 1 (greigite) only occurs between 200 and 500 mbsf, contributing most to the magnetic signal up to 0.76 (Figure 6a). Below 500 mbsf, EM 2 (fine-grained magnetite) is the mineral phase with the highest contribution between 0.66 and 1 (Figure 6b). EM 3 (high coercivity minerals) and EM 4 (coarse-grained magnetite) are present in all samples with minor contributions up to 0.31 (Figures 6c and 6d).

#### 4.5. Magnetic Susceptibility

Magnetic susceptibility  $\chi_{lf}$  significantly varies over depth between  $10 \times 10^{-8}$  and  $190 \times 10^{-8} \text{ m}^3 \text{ kg}^{-1}$  with an average value of  $23 \times 10^{-8} \text{ m}^3 \text{ kg}^{-1}$  (Figure 5b). The highest value is observed in the upper Subunit IIA at 200 mbsf. The  $\chi_{lf}$  profile exhibits two distinct maxima between 400 and 500 mbsf and 600 and 900 mbsf.

The  $\text{Fe}_{\text{total}}$  over magnetic susceptibility ratio is used as a proxy for the intensity of magnetite dissolution, whereby high values indicate a loss of fine magnetite (e.g., Funk et al., 2004). In this study,  $\text{Fe}_{\text{total}}$  is compared to the mass-normalized magnetic susceptibility  $\chi_{lf}$  ( $\text{Fe}_{\text{total}}/\chi_{lf}$ ; Figure 5c). The  $\text{Fe}_{\text{total}}/\chi_{lf}$  profile shows the opposite trend compared to  $\chi_{lf}$  with higher values up to 0.5 between 500 and 600 mbsf in Unit III and between 900 and 1,100 mbsf in the lower half of Unit IV.



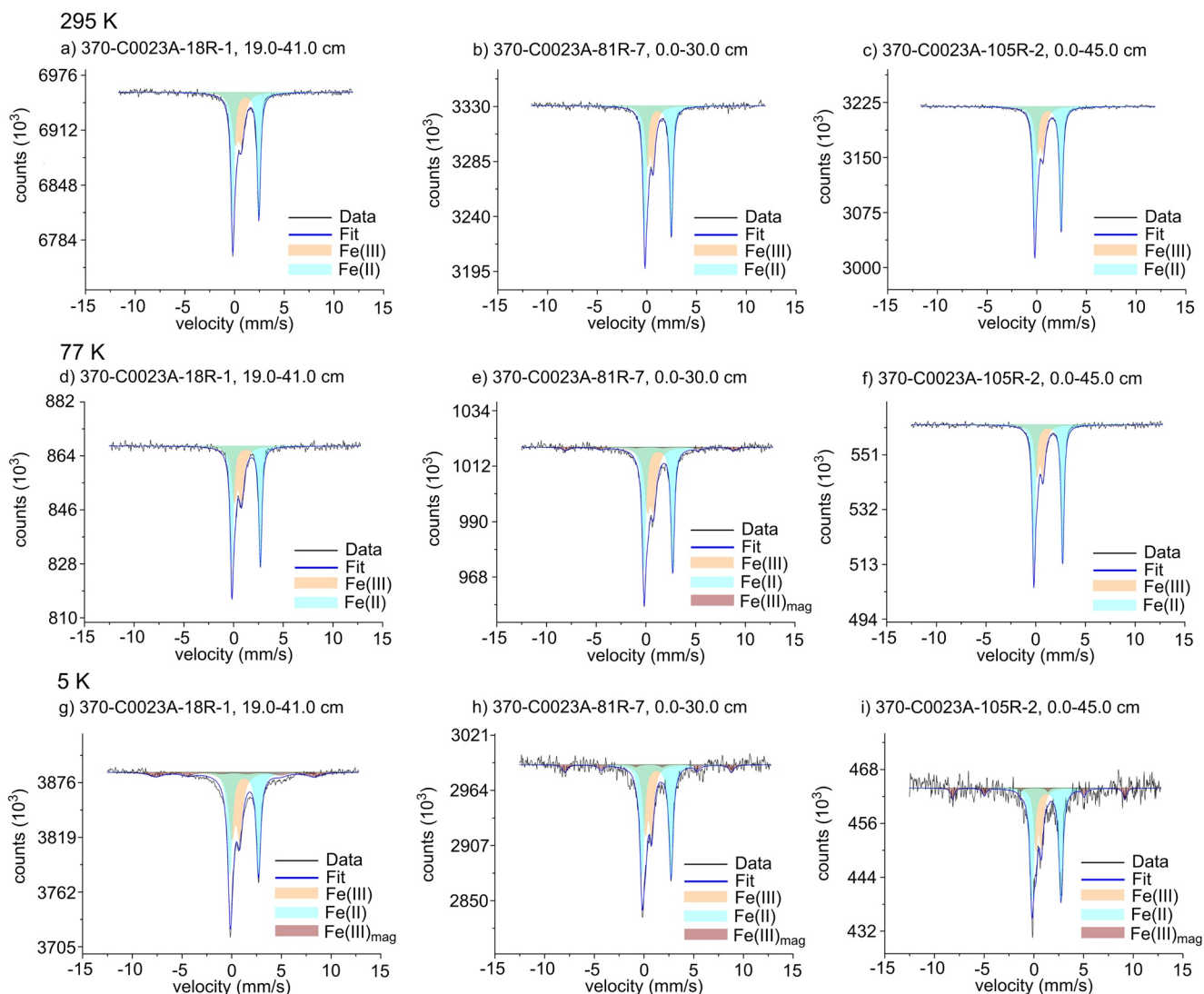


**Figure 7.** Mössbauer spectra collected for each sample at 295 K (a–c), 77 K (d–f), and 5 K (g–i). All samples measured at room temperature (295 K) show a wide doublet which can be attributed to the presence of a non-magnetically ordered Fe(II) phase (light blue). The narrow doublet can be attributed to the presence of an Fe(III) phase (orange). Low-temperature measurements at 5 K confirm the dominant presence of paramagnetic (non-magnetically ordered) Fe(III) mineral phases to be present in all samples likely to represent (clay-sized) Fe-rich phyllosilicates. The absence (or low abundance) of a sextet feature at 5 K suggests the absence (or only low abundance) of magnetically ordered Fe (oxyhydr)oxide phases (Fe(III)<sub>mag</sub>; red) such as hematite, goethite or ferrihydrite; or could be a measuring artefact of a paramagnetic relaxation of Fe atoms in phyllosilicates (details given in the text).

#### 4.6. <sup>57</sup>Fe Mössbauer Spectroscopy

All spectra, collected at room temperature (295 K), generally reveal the dominant presence of a wide doublet (Db1) with a high center shift (CS) ranging from 1.13 to 1.24 mm s<sup>-1</sup> and a relatively high quadrupole splitting ( $\Delta E_Q$ ) of 2.64–2.67 mm s<sup>-1</sup> (Figures 7a–7c; Table S4). These high hyperfine field values for CS and  $\Delta E_Q$  are typically indicative of a non-magnetically ordered Fe(II) phase. The relative abundance of this Fe(II) phase is <60% in all samples (Table S4). The asymmetry in all collected spectra and the bump on the left shoulder indicate the presence of an additional spectral feature, which is designated in the model-fit as Db2 (Figures 7a–7c). The hyperfine field parameters for Db2 show generally lower values for CS ranging from 0.35 to 0.37 mm s<sup>-1</sup> and  $\Delta E_Q$  from 0.57 to 0.64 mm s<sup>-1</sup>, suggestive for an Fe(III) phase. All samples have a higher relative abundance of Fe(II) over Fe(III) (Table S4).

While the spectra collected at 77 K for samples 370-C0023A-18R-1, 19.0–41.0 cm and 370-C0023A-105R-2, 0.0–45.0 cm only show the dominant doublet features (Figures 7d and 7f), a poorly defined sextet (S1) in

the spectrum of sample 370-C0023A-81R-7, 0.0–30.0 cm, points to the presence of a more crystalline, partly magnetically ordering Fe phase with a relative abundance of ~6% (Figure 7e and Table S4). However, the hyperfine field values of S1 do not allow a clear identification of the mineral phase (e.g., goethite or hematite).

Spectra recorded at 5 K still show the very dominant doublet features as being detected at higher temperatures (Figures 7g–7i). The relative abundance for Fe(II) over Fe(III) ranges from 49% (370-C0023A-18R-1, 19.0–41.0 cm) to 61% (370-C0023A-105R-2, 0.0–45.0 cm; Table S4). In the background of all spectra collected at 5 K, a poorly defined sextet feature is visible. This rather collapsed sextet indicates the presence of an Fe phase which was starting to undergo magnetic ordering at 5 K.

## 5. Discussion

### 5.1. Quantification and Characterization of Reactive Fe Mineral Phases at Site C0023

The average  $Fe_{total}$  content at Site C0023 (Figure 3a) is in the range of bulk Fe contents in sediments from the Kumano Transect of the Nankai Trough (IODP Site C0012), located off Kii Peninsula ~200 km north-east of the Muroto Transect (~4 wt%; Torres et al., 2015). The hydroxylamine-HCl-leachable Fe fraction, typically comprised of labile Fe (oxyhydr)oxides ( $Fe_{hyam}$ ) including ferrihydrite and lepidocrocite (Poulton & Canfield, 2005), dominated the fractions of extractable Fe at Site C0023 (Figure 4b). According to Canfield et al. (1992) and Poulton et al. (2004), ferrihydrite and lepidocrocite undergo reductive dissolution driven by microbial degradation of organic matter and reactions with hydrogen sulfide on timescales from minutes to days, respectively. Considering the age (up to ~15 Ma) and temperature of the sediments at Site C0023, labile Fe (oxyhydr)oxides are unlikely to be preserved in these ancient sediments. Even though low organic carbon contents during deposition of Unit IV might have been insufficient to drive dissimilatory Fe reduction, which could have led to a preservation of reactive Fe (oxyhydr)oxides (e.g., Riedinger et al., 2005, 2014; see Section 5.2.1), ferrihydrite and lepidocrocite would have been converted to more crystalline Fe oxides such as goethite, especially over timescales of several million years (e.g., Cornell & Schwertmann, 2003). Therefore, the extraction data seemed suspicious in terms of the conventional interpretation of the  $Fe_{hyam}$  fraction and was further investigated.

Recent studies by Slotznick et al. (2020) and Hepburn et al. (2020) focused on the efficiency of Fe chemical sequential extractions to dissolve the target phases. Both studies showed that the hydroxylamine-HCl step after Poulton and Canfield (2005) effectively extracts easily reducible Fe (oxyhydr)oxides when present. However, Hepburn et al. (2020) also demonstrated that nontronite, an Fe(III)-rich member of the smectite group, is also dissolved during the hydroxylamine-HCl step. Ryan et al. (2008) further observed a partial dissolution of Fe contained in chlorite and smectite of up to 13.5% of bulk Fe even with a less concentrated hydroxylamine-HCl solution (0.5 M) and a shorter reaction time of only 16 h. The hydroxylamine-HCl treatment leads to the reduction of structural Fe(III) in these phyllosilicates, which creates local instabilities in crystal energies from charge imbalance, thus, promoting mineral dissolution (Stucki et al., 1984). The study by Slotznick et al. (2020) further showed that  $NH_4$ -oxalate appears to solubilize Fe-bearing silicates, specifically berthierine and chamosite.

Phyllosilicates, including the clay minerals chlorite and smectite are abundant at Site C0023, especially in the Lower Shikoku Basin formation (Heuer et al., 2017a). The total clay mineral contents obtained from XRD analyses gradually increase from Subunit IIA towards the sediment-basement interface and is, thus, proportional to the  $Fe_{hyam}$  profile (Figure 4b). Aluminum (Al) and silicon (Si) are main components of Fe-rich phyllosilicates including nontronite, chlorite and biotite. In order to examine if Fe bound in phyllosilicates is unintentionally dissolved during the applied Fe sequential extraction, we compared the amounts of Al and Si to Fe released by the different extraction steps for a selection of 16 samples (Figure S4). Our data show very good correlation between  $Fe_{hyam}$  and  $Al_{hyam}$  ( $R^2 = 0.91$ ) and  $Fe_{oxa}$  and  $Al_{oxa}$  ( $R^2 = 0.98$ ) and slightly lower correlation between  $Fe_{hyam}$  and  $Si_{hyam}$  ( $R^2 = 0.70$ ) and  $Fe_{oxa}$  and  $Si_{oxa}$  ( $R^2 = 0.75$ ). In addition, the Mössbauer spectroscopy analysis strengthens our hypothesis. The presence of the dominant doublet features in all collected spectra and the prevalent non-magnetic (paramagnetic) behavior at 5 K can be attributed to a high abundance (>85%) of phyllosilicates in all three samples (Figure 7). The hyperfine parameters of the collapsing sextet feature in all spectra at 5 K could be attributed to a poorly crystalline

Fe(III) (oxyhydr)oxide such as ferrihydrite, goethite or even hematite to be present by <15%. However, this collapsing sextet feature might also reflect an artifact of paramagnetic relaxation of Fe atoms at around 5 K, which can create sextets in the absorbance spectra with similar hyperfine parameters. This effect has been previously shown in phyllosilicates containing low Fe contents (Murad, 1998). From this, we deduce that the most prevalent Fe mineral phase in the analyzed samples are mixed-valent Fe-rich, potentially clay-sized, phyllosilicates and the easily reducible Fe(III) (oxyhydr)oxides ferrihydrite and lepidocrocite are absent or only present in very small quantities. Since clay-sized phyllosilicates are hardly monomineralic, it needs to be considered that multiple Fe-phyllosilicate fractions are abundant in these samples. Current Mössbauer spectroscopy results do not allow a clear distinction between different clay fractions. However, the hyperfine parameters for most of the recorded spectra point towards kaolinite ( $\text{Al}_2\text{Si}_2\text{O}_5(\text{OH})_4$ ) to be a relatively abundant candidate which usually occurs with a minor substitution of Fe for Al (Murad, 1998). The appearance of kaolinite was also confirmed by XRD analyses (Kim et al., 2019).

The positive correlation between Al and Fe as well as Si and Fe in the hydroxylamine-HCl and  $\text{NH}_4$ -oxalate fractions in combination with the Mössbauer spectroscopy data imply a partial dissolution of phyllosilicates and the remobilization of both the sheet layer matrix components (Al and Si) and substituted Fe atoms in the octahedral (Fe[II] and Fe[III]) and tetrahedral (Fe[III]) sites. Therefore, the high  $\text{Fe}_{\text{hyam}}$  contents at Site C0023 do not indicate the presence of Fe (oxyhydr)oxides such as ferrihydrite and lepidocrocite, but rather represent structural Fe(III) contained in phyllosilicates that survived complete reductive dissolution. Current studies indicate that structural Fe(III) in phyllosilicates can be reduced microbially (e.g., Jung et al., 2019; Kim et al., 2004; Vorhies & Gaines, 2009), although this Fe pool is thought to be reactive only on timescales of  $10^2$ – $10^5$  of years (Canfield et al., 1992). More recently, Kim et al. (2019) showed that microbial reduction of structural Fe(III) in smectite promotes the smectite-to-illite transition at Site C0023 even at relatively low temperature and pressure conditions. Thus, the hydroxylamine-HCl-extracted Fe pool represents the part of phyllosilicate Fe(III) that has been preserved during burial and can support microbial Fe reduction as suggested by Kim et al. (2019).

Magnetic techniques are great complements to geochemical analyses as they provide independent information on Fe mineralogy, which allows a better Fe speciation interpretation. Here, the combination of the sequential extraction of Fe (oxyhydr)oxides and sulfides with IRM acquisition curves improves the characterization of the Fe mineral assemblages at Site C0023. The coercivity unmixing shows that fine-grained magnetite (EM 2) is the main carrier of the magnetic signal between 600 and 900 mbsf (Figure 6b), coinciding with higher  $\text{Fe}_{\text{di-ct}}$  values (Figure 4c). Furthermore, this zone of elevated  $\text{Fe}_{\text{di-ct}}$  contents is also supported by higher magnetic susceptibility, suggesting that fine-grained magnetite is largely dissolved during the Na-dithionite step. These findings are in agreement with Henkel et al. (2016), Oonk et al. (2017) and Slotznick et al. (2020), who observed a grain-size dependent dissolution of magnetite of up to 75% during the Na-dithionite step after Poulton and Canfield (2005).

To conclude, while  $\text{Fe}_{\text{hyam}}$  and  $\text{Fe}_{\text{oxa}}$  extracted some of the Fe bound in phyllosilicates,  $\text{Fe}_{\text{di-ct}}$  extracted crystalline Fe (oxyhydr)oxides, mainly goethite, hematite and fine-grained magnetite. Our analyses demonstrate that Fe speciation on ancient sediments must be interpreted with caution. As already proposed by Slotznick et al. (2020) and Hepburn et al. (2020), the application of an independent technique such as rock magnetic analyses or Mössbauer spectroscopy on selected samples is very useful to validate chemical Fe extraction data. The Poulton and Canfield (2005) method was tested on modern fluvial and glacial sediments. Thus, if applying this methodology on ancient sediments, the protocol needs to be verified and modified to the specific set of samples prior to the analyses.

## 5.2. Evolution of Biogeochemical and Diagenetic Processes at Site C0023

During its tectonically induced movement from the Shikoku Basin to the Nankai Trough (e.g., Mahony et al., 2011; Underwood & Guo, 2018; Figure 1), Site C0023 has experienced a transition from hemipelagic basin-style to trench-style deposition, accompanied by significant changes in thermal conditions and resulting (bio-)geochemical processes. Abyssal sediments are generally characterized by low sedimentation rates and organic carbon contents (<1 wt%) that are insufficient to drive organoclastic Fe and sulfate reduction (e.g., D'Hondt et al., 2015; Mewes et al., 2014; Mogollón et al., 2016; Volz et al., 2018). Nonetheless, diagenetic mineral phases including pyrite (Figure 3d), accompanied by minima in magnetic susceptibility

(Figure 5b) and Fe oxide contents (Figure 4c), are observed in the whole sediment column at Site C0023 (Figure 3d)—even in the lowermost carbon-starved unit. This suggests that redox and sulfidation fronts have changed post-depositionally during the past 15 Ma. High methane concentrations in the Upper Shikoku Basin formation (Unit III) and concurrently low present-day potential methanogenesis rates (Heuer et al., 2020) further suggest that redox dynamics and related microbial activities were markedly different in the past. In the following, the succession of biogeochemical and diagenetic processes as derived from pore-water and solid-phase records that affected the sedimentary Fe pool at Site C0023 from deposition through progressing burial and diagenetic alteration to the present-day situation will be outlined.

### 5.2.1. Organic Carbon-Starved, Low Sedimentation Environment

The deposition of the Lower Shikoku Basin formation (Unit IV) began in the middle Miocene (13.53 Ma), ~750 km away from its current location (Figure 1), and lasted until Pliocene times (2.53 Ma), whereby the prevailing sedimentation rates slightly increased from 3.5 to 6.0 cm kyr<sup>-1</sup> (Hagino & the Expedition 370 Scientists, 2018). The modern Pacific Ocean circulation established ~14 Ma (Kuhnt et al., 2004). The Shikoku Basin sedimentation is strongly affected by the Kuroshio Current (KC), which represents the western boundary current as part of the North Pacific subtropical gyre (e.g., Qui, 2001). The KC is characterized by nutrient-poor, oligotrophic conditions (e.g., Guo, 1991; Hirota, 1995), and thus, causes low primary productivity and particulate organic carbon (POC) fluxes in surface waters of the Shikoku Basin. Low TOC/N ratios ( $\leq 10$ ) and  $\delta^{13}\text{C}$ -TOC values between  $-23\text{‰}$  and  $-22\text{‰}$  in Unit IV (Figures S2a and S2b) point to organic matter of marine origin (e.g., Meyers, 1994). Alkenones, which are biomarkers for coccolithophores (haptophyte algae) are only present in low concentrations in the Lower Shikoku Basin formation above 860 mbsf when compared to the Upper Shikoku Basin formation, and long-chain diols, biomarkers for eustigmatophyte algae, are absent (Figures S2c and S2d). The  $\delta^{13}\text{C}$ -TOC and TOC/N data in combination with low alkenone and diol concentrations are indicative of an oligotrophic setting. Notably, we cannot exclude that with the onset of catagenetic processes at ~70°C below 600 mbsf (Tsang et al., 2020), thermal degradation of organic matter may also lead to a decline in biomarker concentrations in Unit IV, however, we would expect this decline to be more gradual and not as abrupt as is observed within Unit III.

The combination of relatively low sedimentation rates with low POC fluxes conceivably led to low carbon burial rates and accordingly low TOC contents during the deposition of Unit IV (~0.25 wt%, Figure 5a). Therefore, a carbon-starved, low sedimentation depositional environment characterizes the sediments from late Miocene to Pliocene times. In these organic carbon-lean abyssal ocean type sediments, organic matter mineralization is typically dominated by aerobic respiration and nitrate reduction leading to a high TOC degradation efficiency (e.g., Emerson et al., 1980; Froelich et al., 1979; Mogollón et al., 2016; Volz et al., 2018). The very low preserved TOC contents of ~0.25 wt% were insufficient to drive organoclastic Fe and sulfate reduction (e.g., Riedinger et al., 2014). Hence, between 15 and 2.5 Ma, pore-water sulfate was likely not depleted and could penetrate deep into the sediments of Unit IV at Site C0023 and buried Fe (oxyhydr)oxides were not affected by reductive dissolution (Figure 8a).

Due to high heat flow prevailing in the studied area (Harris et al., 2013), the temperature at the sediment-basement interface was ~40°C during the deposition of the Lower Shikoku Basin formation. The sediment temperature steadily increased with ongoing burial (Horsfield et al., 2006; Tsang et al., 2020). As Site C0023 continuously moved in northwesterly direction towards the Japanese Island arc, the lithology changed from Lower to Upper Shikoku Basin formation at ~2.5 Ma, accompanied by an increase in sedimentation rate to 9.3 cm kyr<sup>-1</sup> (Hagino & the Expedition 370 Scientists, 2018). TOC contents in the latter unit (Unit III) show an increasing trend compared to Unit IV (Figure 5a), which could be caused by an overall increase in primary productivity during the late Pliocene-early Pleistocene transition or a better preservation due to higher sedimentation rates (e.g., Lawrence et al., 2013; Swann et al., 2006; Zonneveld et al., 2010). Berner and Koch (1993) and Shipboard Science Party (2001) further pointed out that a steady increase in the amount of organic carbon in the transition from the Lower to the Upper Shikoku Basin formation at the adjacent Sites 808 and 1174 of Ocean Drilling Program (ODP) Legs 131 and 190, respectively, may be related to higher nutrient supply caused by the proximity to the coast of Japan. In addition, an intensification of the KC that has occurred in response to the closure of the Central America Seaway at ~3 Ma (e.g., Molina-Cruz, 1997; Tsuchi, 1997) could have increased the nutrient supply from the Japanese Island arc (Underwood & Steurer, 2003). The  $\delta^{13}\text{C}$ -TOC and algal biomarker data support elevated marine



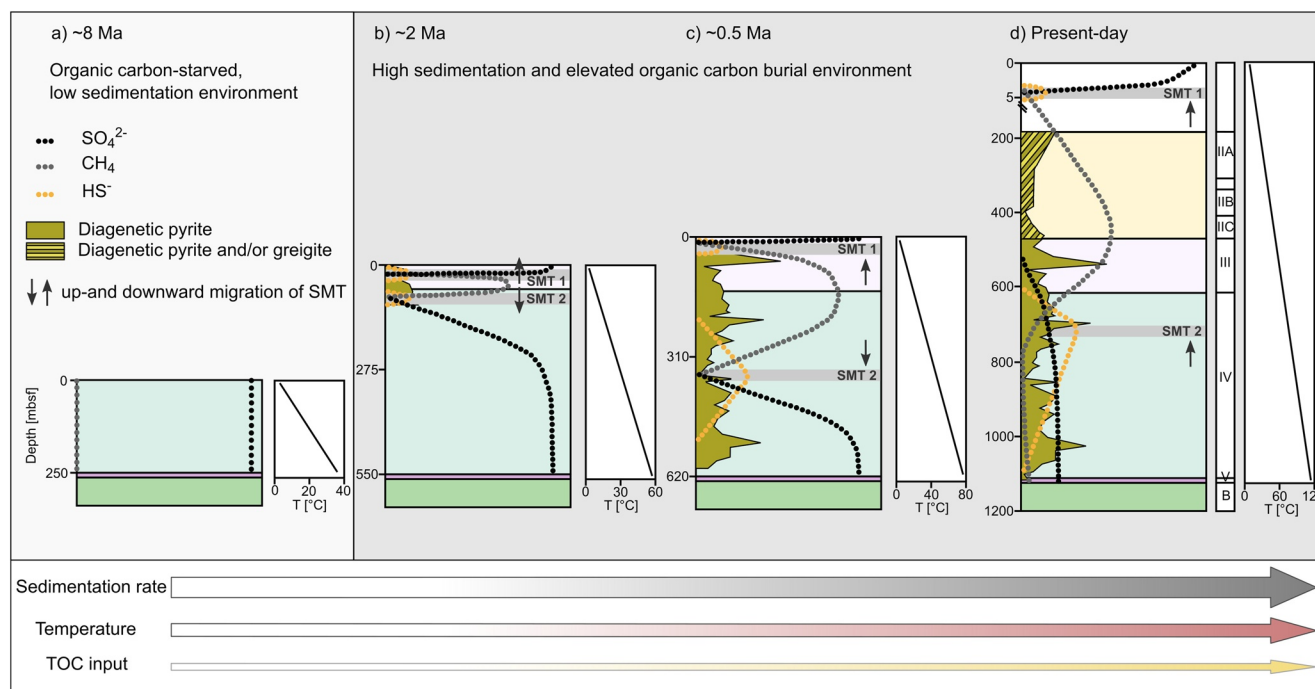


**Figure 8.** Conceptual model showing the evolution of biogeochemical and diagenetic processes at Site C0023 during its tectonic migration over the past 15 Ma. The main driving force for changes in the (bio-)geochemical processes is the significant increase in sedimentation rate which in turn also affects the temperature within the sediment column and the total organic carbon burial. The more intense color shading of each arrow indicates the increase of the respective driving force. These changes in depositional, thermal, and geochemical conditions led to a transition from (a) an organic carbon-starved sedimentary environment with comparably low accumulation rates to (b) an environment with elevated sedimentation and carbon burial rates. Increasing sedimentation and organic carbon burial rates since ~2.5 Ma likely caused the onset of methanogenesis and anaerobic oxidation of methane (AOM) and the formation of a shallow and a lower sulfate-methane transition (SMT) (SMT 1 and SMT 2, respectively).  $\text{HS}^-$  produced by AOM reacted with solid-phase and dissolved Fe to form pyrite. (c) The arrival of Site C0023 at the Nankai Trough at ~0.5 Ma, accompanied by a significant increase in sediment temperature could have resulted in enhanced methanogenesis, likely due to increased bioavailability of organic matter and the up- and downward migration of the SMTs and sulfidization fronts. (d) Present-day situation with the shallow SMT 1 at ~4 mbsf (assumed from ODP Site 1174; Shipboard Science Party, 2001) and the lower SMT 2 at ~730 mbsf. Extremely high sedimentation rates since 0.43 Ma prevented a complete pyritization and the preservation of greigite.

productivity during the deposition of the Upper Shikoku Basin formation. The increase in TOC contents is accompanied by a shift of  $\delta^{13}\text{C}$ -TOC towards more positive values in Unit III (Figure S2b). Periods of high primary productivity typically lead to an increased uptake of  $^{12}\text{C}$ , whereby the residual inorganic carbon becomes increasingly enriched in  $^{13}\text{C}$ , ultimately resulting in more positive  $\delta^{13}\text{C}$  values of the preserved sedimentary organic matter (e.g., Meyers, 1997; Mizutani & Wada, 1982). At the same time, alkenone and long-chain diol concentrations significantly increase in Unit III (Figures S2c and S2d), which is consistent with an increased productivity and thus, elevated POC fluxes. We suggest that the concurrent increase in sedimentation and TOC burial rates at ~2.5 Ma has caused a transition from an organic carbon-starved sedimentary system with comparable low accumulation rates ( $3.5 \text{ cm kyr}^{-1}$ ) to an environment with elevated sedimentation ( $9.3 \text{ cm kyr}^{-1}$ ) and carbon burial rates at the Pliocene-Pleistocene boundary.

### 5.2.2. Elevated Organic Carbon Burial, High Sedimentation Environment

Higher carbon burial rates since the early Pleistocene could have stimulated the establishment of anoxic sediment conditions, and thus, triggered the onset of organoclastic Fe and sulfate reduction and biogenic methane formation in the deposits of Unit III (Figure 8b). Once produced in Unit III, methane was subsequently oxidized by sulfate present in the pore water during the anaerobic oxidation of methane (AOM). As methane further diffused up- and downwards, both a shallow and a deep or inverse sulfate-methane transition (SMT) were formed: (1) the shallow SMT must have formed within Unit III where upward diffusing methane reacts with sulfate diffusing downwards from the overlying seawater. (2) The reaction of downward diffusing methane with residual, upward diffusing sulfate in Unit IV resulted in the establishment of the lower inverse SMT. AOM releases hydrogen sulfide and bicarbonate into the pore water (e.g., Barnes &

Goldberg, 1976; Borowski et al., 1996; Niewöhner et al., 1998), which also diffuse up- and downwards. At the SMTs, hydrogen sulfide reacted either with preserved Fe (oxyhydr)oxides or with  $\text{Fe}^{2+}$  in the upper part of Unit III, where TOC contents were high enough to drive organoclastic Fe reduction, to form pyrite (e.g., Berner, 1970).

Site C0023 reached the Nankai Trough  $\sim 0.5$  Ma ago (Figure 1). The resulting transition from a hemipelagic basin-style to a trench-style deposition led to a pronounced increase in sedimentation rates of one order of magnitude (Figure 5d), accompanied by a temperature increase of about  $50^\circ\text{C}$  across the sediment column (Horsfield et al., 2006; Tsang et al., 2020). Several studies on deep seafloor sediments show that organic matter that is highly refractory at seafloor temperature ( $\sim 2\text{--}3^\circ\text{C}$ ) becomes accessible for microbial processes with increasing burial and related heating of the sediments (Burdige, 2011; Parkes et al., 2007; Wellsbury et al., 1997). Riedinger et al. (2015) suggested that frictional heating associated with earthquakes might reactivate recalcitrant organic matter in deep sediments from IODP Sites C0006 and C0008 in the Nankai Trough, resulting in the onset of methanogenesis several hundred meters below the seafloor. Although, we cannot provide evidence on the reactivity of the organic material, we hypothesize that the higher temperatures prevailing since  $\sim 0.5$  Ma increased the bioavailability of organic matter at Site C0023, which caused enhanced rates of biogenic methanogenesis and higher methane fluxes in both, up- and downward directions. The assumption that the increased methane concentrations in Unit III are related to enhanced microbially mediated methanogenesis and not to thermogenic methane production is further supported by the stable carbon isotopic composition of methane ( $\delta^{13}\text{C}\text{-CH}_4$ ). The  $\delta^{13}\text{C}\text{-CH}_4$  values in the methane-rich zone between 200 and 600 mbsf varies between  $-60\%$  and  $-65\%$  (Figure S2f), which is indicative of a biogenic methane source (Heuer et al., 2020). Furthermore, as evidenced by increasing  $\delta^{13}\text{C}\text{-CH}_4$  values and concurrently decreasing methane/ethane ratios ( $C_1/C_2 < 10^3$ ; Figure S2e), thermogenic methane produced by thermal degradation of the organic matter provides an additional source of methane from below (Heuer et al., 2017a, 2020). These increased methane fluxes, in turn, could cause an up- and downward migration of the shallow and inverse SMT, respectively, and simultaneously slow prograding shifts of the sulfidization fronts (Figure 8c). In this way, the lower sulfidization front could shift into the Lower Shikoku Basin formation, leading to an alteration of the preserved sedimentary Fe pool and the formation of diagenetic pyrite several millions of years after initial deposition. This proposed scenario is confirmed by the magnetic and sequential extraction data: while  $\text{Fe}_{\text{di-cr}}$  contents (Figure 4c) and magnetic susceptibility (Figure 5b) values show minima in the lower parts of Unit IV, CRS contents are enriched (Figure 3d), indicating that ferrimagnetic Fe oxides such as hematite and magnetite are converted into paramagnetic pyrite. Concurrently, high  $\text{Fe}_{\text{total}}/\chi_{\text{if}}$  ratios indicate intense reductive magnetite dissolution (Funk et al., 2004; Korff et al., 2016; Figure 5c). Furthermore, all three samples analyzed by Mössbauer spectroscopy show relative abundances for Fe(II) over Fe(III) and thus, relatively high Fe(II)/Fe(III) ratios (Table S4). This suggests that the phyllosilicates at Site C0023 have experienced microbial or abiotic reduction (Stucki et al., 1996) which led to the reduction of Fe(III) and the formation of Fe(II) in the sheet layers as reported for Fe-rich phyllosilicates in marine sediments from the continental shelf off the Antarctic Peninsula (Jung et al., 2019). High Fe(II)/Fe(III) ratios even in the deeper samples from Unit IV are in agreement with the described shift of redox fronts.

The results of coercivity unmixing (Figures 6 and S3) indicate the occurrence of greigite down to  $\sim 460$  mbsf. Greigite ( $\text{Fe}^{2+}\text{Fe}^{3+}_2\text{S}_4$ ) is a meta-stable ferrimagnetic Fe sulfide that forms as a precursor of pyrite (e.g., Berner, 1984; Fu et al., 2008; Jørgensen et al., 2004; Kasten et al., 1998; Sweeney & Kaplan, 1973; Wilkin & Barnes, 1996). The occurrence of greigite correlates with the significant increase in sedimentation rates since 0.29 Ma (Figure 5d; Hagino & the Expedition 370 Scientists, 2018). A complete pyritization might have been prevented by decreasing the time the respective interval was located in the sulfidic zone, and thus, greigite is preserved in Subunits IIA and IIB (e.g., Fu et al., 2008; Jørgensen et al., 2004; Kasten et al., 1998; Riedinger et al., 2005). Authigenic growth of ferrimagnetic greigite has important implications for paleomagnetic recording (e.g., Roberts, 2015) as its formation leads to a secondary increase in the magnetic signal. Therefore, high  $\chi_{\text{if}}$  values in Subunit IIA (Figure 5b) are probably caused by the preservation of greigite.

In the present-day situation, the interval between 600 and 700 mbsf - located above the lower SMT - is both sulfide- and  $\text{Fe}^{2+}$ -free, suggesting that upward diffusing hydrogen sulfide currently reacts with downward diffusing  $\text{Fe}^{2+}$  to form Fe sulfides (Figures 2b and 2c). Downward diffusing sulfide from the lower SMT

might still react with residual Fe oxides and/or phyllosilicate-bound Fe(III) in the lower parts of Unit IV to form pyrite (Figure 8d). Shallow sediments (<189 mbsf) were not recovered during IODP Expedition 370. However, based on sulfate and methane data from the adjacent ODP Leg 190 Site 1174 (Shipboard Science Party, 2001), the present-day shallow SMT is assumed to be located between 3 and 4.5 mbsf. Cell concentrations at Site C0023 are two to four orders of magnitude lower compared to other continental margin sub-seafloor sediments, leading to methanogenesis rates below the typical range in marine sediments (Heuer et al., 2020), and hence, generally low DIC concentrations (Figure 2d). Due to the decreased methane flux, the lower inverse SMT migrated upwards to its current position at ~730 mbsf. At the same time, high temperature prevailing at and below the inverse SMT likely exert an important control on the expansion of the AOM zone, and thus, the location of the SMT. The current depth of the lower inverse SMT corresponds to a temperature of ~80–85°C. A sharp increase towards higher  $\delta^{13}\text{C-CH}_4$  values (up to  $-54\text{‰}$ ) at this depth (Figure S2f) indicates a biogenic methane sink and the activity of AOM-performing communities (Heuer et al., 2020). This temperature range overlaps with the known maximum growth temperature of ~70°C for methane-oxidizing communities based on in vitro incubation experiments and AOM activity at in situ temperatures up to 90°C in hydrothermally influenced sediments from the Guaymas Basin, Gulf of California (Biddle et al., 2012; Holler et al., 2011). Therefore, microbial AOM potentially only barely occurs at present, which results in the observed broad overlap of methane and sulfate and the presence of methane down to the basement (Figure 2a).

### 5.3. Implications for the Interpretation of Deep Subseafloor Pore-Water and Sedimentary Records

The described succession of the biogeochemical and diagenetic processes has been summarized in a conceptual geochemical process model (Figure 8). The main driving forces for the evolution of the (bio-)geochemical processes at Site C0023 are the sedimentation rate, the temperature within the sediment, and the TOC input. During the migration from the Shikoku Basin towards the Nankai Trough, the sediments at Site C0023 have experienced a significant increase in sedimentation rates from 3.5 cm kyr<sup>-1</sup> in the lower parts of Unit IV to 131.9 cm kyr<sup>-1</sup> in Unit IIB (Table 1; Hagino & the Expedition 370 Scientists, 2018). The sedimentation rate is strongly interrelated with the sedimentary temperature and the TOC burial. Since the temperature within the sediment column at Site C0023 is a function of heat flow, thermal conductivity, and the sediment depth below seafloor (Heuer et al., 2020), it rose with ongoing burial. Similarly, the TOC contents increased when Site C0023 moved towards Japan. These changes in depositional, thermal, and geochemical conditions resulted in a transition from oxic (Figure 8a) to anoxic conditions within the sediments and the onset of anaerobic terminal electron-accepting processes (Figure 8b). Higher methane fluxes at ~0.5 Ma caused an up- and downward migration of the SMTs and sulfidization fronts, and thus, promoted the transformation of Fe (oxyhydr)oxides into pyrite in the underlying Lower Shikoku Basin formation several millions of years after the initial sediment deposition (Figure 8c). We do not imply that the up- and downward migration of the lower SMT in Unit IV (Figures 8c and 8d) was due to a migration of the microbial community performing AOM through 150–200 mbsf of consolidated sediment, but we rather assume a long-term survival of microbes (e.g., Inagaki et al., 2015). Comparable observations were made by Arndt et al. (2006), who showed that organic-rich layers in subseafloor sediments at Demerara Rise in the equatorial Atlantic (ODP Leg 207, Site 1258) still provide a suitable substrate for ongoing methane formation in the deep biosphere almost 100 Ma after their deposition, thereby controlling the element fluxes and biogeochemical processes within the whole overlying sediment column. Similarly, the primary sediment composition in the Lower Shikoku Basin formation at Site C0023 is significantly overprinted by the onset of methanogenesis and AOM in the overlying Upper Shikoku Basin formation.

Over a long period (15–2.5 Ma), the pore-water sulfate concentrations in the Lower Shikoku Basin formation were comparable with seawater values (~28 mM) due to the absence of organoclastic sulfate reduction during deposition. The lower inverse SMT could have been formed only due to the availability of this sulfate pool preserved at greater depth. The sulfate concentrations continuously decreased since the onset of AOM at ~2.5 Ma. At present, the deep residual sulfate pool is almost exhausted by AOM (<7 mM; Figure 2a). This finding indicates that the present-day sulfate profile is strongly influenced by (bio-)geochemical processes occurring in the overlying sediments. Thus, in order to avoid a misinterpretation of the origin of the low sulfate in the Lower Shikoku Basin formation, it is crucial to consider the (bio-)geochemical history of Site

C0023. A similar consideration applies for methane. Highest methane concentrations are observed in an interval, where cells were not detectable (Heuer et al., 2020). At the same time, present-day methanogenesis rates are low, suggesting that microbial activities and (bio-)geochemical processes were significantly different in the past. Therefore, our study demonstrates that the pore-water patterns we observe today are strongly correlated with the succession and past evolution of the (bio-)geochemical processes at Site C0023. Elevated sulfate concentrations at greater depth and a lower inverse SMT were also observed at IODP Site C0012 (Torres et al., 2015), which is located on the Kashinosaki Knoll—an isolated seamount of volcanic origin on the subducting Philippine Sea plate—in the Kumano Transect (Ike et al., 2008). However, due to its location on a basement high and a significant reduced sediment thickness, the depositional and geochemical conditions are different compared to Site C0023. Chloride concentrations at Site C0012 significantly increase above a typical seawater value of 558 mM below 300 mbsf until the sediment-basement interface. Thus, the observed increase in sulfate concentrations with depth at Site C0012 is likely not related to a relict sulfate pool but attributed to a diffusional sulfate supply from the basement aquifer (Torres et al., 2015; Underwood et al., 2010). This comparison demonstrates that the sedimentary packages in the Nankai-Shikoku-subduction system are exposed to different geochemical controls even on comparably small-scale spatial distances. Nonetheless, following our conceptual model (Figure 8), a relict sulfate pool should be considered when interpreting sulfate concentrations in subseafloor sediments from the Nankai Trough and the incoming Shikoku Basin.

## 6. Conclusions

We studied deep subseafloor sediments from Site C0023 offshore Japan in the Nankai Trough, northwest Pacific Ocean drilled during IODP Expedition 370. During its tectonic migration from the Shikoku Basin to the Nankai Trough, Site C0023 has experienced significant changes in depositional and thermal conditions as well as resulting biogeochemical processes over the past 15 Ma. By combining a large set of complementary pore-water, solid-phase, and rock magnetic data with sedimentation rates and sediment ages, we derived a conceptual geochemical process model that shows the potential succession of biogeochemical processes, element fluxes, and the associated diagenetic overprint of the primary sediment composition.

In summary, the changes in depositional and thermal conditions led to a transition from an organic carbon-starved environment characterized by aerobic respiration and a deep sulfate penetration to elevated carbon burial and the onset of organoclastic Fe and sulfate reduction, biogenic methanogenesis, and AOM at ~2.5 Ma. Increased biogenic methane production presumably caused by a pronounced temperature increase at ~0.5 Ma likely resulted in higher methane fluxes and an up-and downward migration of the SMTs and the sulfidization fronts. Due to the downward migration of the sulfidization front into the lower organic carbon-starved sediments, the preserved Fe (oxyhydr)oxides were diagenetically transformed into pyrite several millions of years after initial deposition of these sediments.

While the combination of chemical and rock magnetic Fe speciation methods with  $^{57}\text{Fe}$  Mössbauer spectroscopy analysis generally allows a better quantification and characterization of the reactive Fe pool at Site C0023, our analyses also demonstrate that Fe speciation data need to be interpreted with caution if applying chemical sequential Fe extraction on ancient sediments such as in this study. Thus, we recommend a cross-check with Al and Si or, even better, the application of a secondary independent Fe speciation technique on a selection of samples. Our results indicate that high amounts of reducible Fe(III) are present in phyllosilicates and can potentially serve as electron acceptor for microbial Fe reduction in the deep subseafloor sediments at Site C0023.

Our study emphasizes that depositional and thermal changes ultimately driven by the tectonically induced migration have the potential to strongly influence (bio-)geochemical processes and element fluxes within the whole sediment column. Thus, to ensure a proper use and interpretation of sedimentary records it is crucial to consider the geological background and the (bio-)geochemical history of deep subseafloor sediments. Such studies are indispensable to gain a fundamental understanding of the coupling between depositional history, biogeochemical processes and the resulting diagenetic overprint on geological timescale, thereby linking the sedimentary Fe, S, and C cycles.



## Conflict of Interest

The authors declare no conflicts of interest relevant to this study.

## Data Availability Statement

Additional data and figures relevant for this study are provided in the Supporting Information or archived in the World Data Center PANGAEA via <https://doi.org/10.1594/PANGAEA.930858> (solid-phase geochemistry; Köster et al., 2021a), <https://doi.org/10.1594/PANGAEA.929317> (rock magnetic end-member unmixing; Köster et al., 2021b) and <https://doi.pangaea.de/10.1594/PANGAEA.929380> (magnetic susceptibility; Kars & Köster, 2021).

## Acknowledgments

This research used samples and data provided by the International Ocean Discovery Program (IODP). The authors would like to thank all personnel involved in the operations aboard the D/V *Chikyu* during Expedition 370, especially Arthur Spivack, Justine Sauvage, Kira Homola, and Yusuke Kubo, as well as the support team at Kochi Core Center. For analytical support in the home laboratory, the authors thank Johann Hollop, Ingrid Stimac, Ingrid Dohrmann, Jenny Wendt, Lea Schabernack, and Oliver Helten. The authors are grateful to Kyoko Hagino for providing sediment ages and sedimentation rates, which were highly beneficial for this study. This work benefited from discussions with Arthur Spivack (University of Rhode Island) and Wolfgang Bach (MARUM, University of Bremen). Finally, the authors thank Nicolas Tribouillard and one anonymous reviewer for their helpful and constructive comments which have significantly improved this manuscript. This study is funded by the German Research Foundation (DFG) in the framework of the priority program 527 (Bereich Infrastruktur—International Ocean Discovery Program; project 388260220). The authors are grateful to the Japan Society for the Promotion of Science (JSPS) and the European Consortium for Ocean Research Drilling (ECORD) for funding Male Köster's research stay at Kochi Core Center in the framework of the JSPS Summer Program 2019 as well as Man-Yin Tsang's research stay at the Alfred Wegener Institute in September 2017, respectively. The authors acknowledge further financial support from the Helmholtz Association (Alfred Wegener Institute Helmholtz Centre for Polar and Marine Research). Myriam Kars's study was supported by the JSPS Grant-in-Aid for Scientific Research (grant 17K05681). Florence Schubotz acknowledges funding by the DFG (project 408178672). Verena B. Heuer further acknowledges support through the DFG (project 387745511) and the Cluster of Excellence "The Ocean Floor—Earth's Uncharted Interface" (project 390741603). Yuki Morono acknowledges funding by the JSPS (19H00730). Additional support enabling this project was provided by the Deep Carbon Observatory. Open access funding enabled and organized by Projekt DEAL.

## References

- Abrajevitch, A., & Kodama, K. (2011). Diagenetic sensitivity of paleoenvironmental proxies: A rock magnetic study of Australian continental margin sediments. *Geochemistry, Geophysics, Geosystems*, 12(5). <https://doi.org/10.1029/2010GC003481>
- Abrajevitch, A., Van der Voo, R., & Rea, D. K. (2009). Variations in relative abundances of goethite and hematite in Bengal Fan sediments: Climatic vs. diagenetic signals. *Marine Geology*, 267(3–4), 191–206. <https://doi.org/10.1016/j.margeo.2009.10.010>
- Arndt, S., Brumsack, H.-J., & Wirtz, K. W. (2006). Cretaceous black shales as active bioreactors: A biogeochemical model for the deep biosphere encountered during ODP Leg 2007 (Demerara Rise). *Geochimica et Cosmochimica Acta*, 70(2), 408–425. <https://doi.org/10.1016/j.gca.2005.09.010>
- Barnes, R. O., & Goldberg, D. E. (1976). Methane production and consumption in anoxic marine sediments. *Geology*, 4(5), 297–300. [https://doi.org/10.1130/0091-7613\(1976\)4%3C297:MPACIA%3E2.0.CO;2](https://doi.org/10.1130/0091-7613(1976)4%3C297:MPACIA%3E2.0.CO;2)
- Becker, K. W., Lipp, J. S., Versteegh, G. M., Wörmer, L., & Hinrichs, K.-U. (2015). Rapid and simultaneous analysis of three molecular sea surface temperature proxies and application to sediments from the Sea of Marmara. *Organic Geochemistry*, 85, 42–53. <https://doi.org/10.1016/j.orggeochem.2015.04.008>
- Berner, R. A. (1970). Sedimentary pyrite formation. *American Journal of Science*, 268, 1–23. <https://doi.org/10.2475/ajs.268.1.1>
- Berner, R. A. (1981). A new geochemical classification of sedimentary environments. *Journal of Sedimentary Research*, 51(2), 359–365. <https://doi.org/10.1306/212F7C7F-2B24-11D7-8648000102C1865D>
- Berner, R. A. (1984). Sedimentary pyrite formation: An update. *Geochimica et Cosmochimica Acta*, 48(4), 605–615. [https://doi.org/10.1016/0016-7037\(84\)90089-9](https://doi.org/10.1016/0016-7037(84)90089-9)
- Berner, U., & Koch, J. (1993). Organic matter in sediments of Site 808, Nankai accretionary prism, Japan. In I. A. Hill, A. Taira, et al. (Eds.), *Proceedings of the ocean drilling program Initial Reports*, 131 (pp. 379–385). College Station, TX: Ocean Drilling Program. <https://doi.org/10.2973/odp.proc.sr.131.132.1993>
- Biddle, F. F., Cardman, Z., Mendlovitz, H., Albert, D. B., Lloyd, K. G., Boetius, A., & Teske, A. (2012). Anaerobic oxidation of methane at different temperature regimes in Guaymas basin hydrothermal sediments. *The ISME Journal*, 6(5), 1018–1031. <https://doi.org/10.1038/ismej.2011.164>
- Boetius, A., Ravenschlag, K., Schubert, C. J., Rickert, D., Widdel, F., Gieseke, A., et al. (2000). A marine microbial consortium apparently mediating anaerobic oxidation of methane. *Nature*, 407(6804), 623–626. <https://doi.org/10.1038/35036572>
- Borowski, W. S., Paull, C. K., & Ussler, W. (1996). Marine pore-water sulfate profiles indicate in situ methane flux from underlying gas hydrate. *Geology*, 24(7), 655–658. [https://doi.org/10.1130/0091-7613\(1996\)024%3C0655:MPWSP1%3E2.3.CO;2](https://doi.org/10.1130/0091-7613(1996)024%3C0655:MPWSP1%3E2.3.CO;2)
- Bowles, M. W., Mogollón, J. M., Kasten, S., Zabel, M., & Hinrichs, K.-U. (2014). Global rates of marine sulfate reduction and implications for sub-seafloor metabolic activities. *Science*, 344(6186), 889–891. <https://doi.org/10.1126/science.1249213>
- Brassell, S., Eglinton, G., Marlowe, I. T., Pflaumann, U., & Sarthain, M. (1986). Molecular stratigraphy: A new tool for climatic assessment. *Nature*, 320(6058), 129–133. <https://doi.org/10.1038/320129a0>
- Burdige, D. J. (2011). Temperature dependence of organic matter remineralization in deeply-buried marine sediments. *Earth and Planetary Science Letters*, 311(3–4), 396–410. <https://doi.org/10.1016/j.epsl.2011.09.043>
- Canfield, D. E., Raiswell, R., & Bottrell, S. H. (1992). The reactivity of sedimentary iron minerals toward sulfide. *American Journal of Science*, 292(9), 659–683. <https://doi.org/10.2475/ajs.292.9.659>
- Canfield, D. E., Raiswell, R., Westrich, J. T., Reaves, C. M., & Berner, R. A. (1986). The use of chromium reduction in the analysis of reduced inorganic sulfur in sediments and shales. *Chemical Geology*, 54(1–2), 149–155. [https://doi.org/10.1016/0009-2541\(86\)90078-1](https://doi.org/10.1016/0009-2541(86)90078-1)
- Canfield, D. E., Thamdrup, B., & Hansen, J. W. (1993). The anaerobic degradation of organic matter in Danish coastal sediments: Iron reduction, manganese reduction and sulfate reduction. *Geochimica et Cosmochimica Acta*, 57(16), 3867–3883. [https://doi.org/10.1016/0016-7037\(93\)90340-3](https://doi.org/10.1016/0016-7037(93)90340-3)
- Chamot-Rooke, N., Renard, V., & Le Pichon, X. (1987). Magnetic anomalies in the Shikoku basin: A new interpretation. *Earth and Planetary Science Letters*, 83(1–4), 214–228. [https://doi.org/10.1016/0012-821X\(87\)90067-7](https://doi.org/10.1016/0012-821X(87)90067-7)
- Cline, J. D. (1969). Spectrophotometric determination of hydrogen sulfide in natural waters. *Limnology & Oceanography*, 14(3), 454–458. <https://doi.org/10.4319/lo.1969.14.3.0454>
- Cornell, R. M., & Schwertmann, U. (2003). Transformations. In R. M. Cornell, & U. Schwertmann (Eds.), *The iron oxides: Structure, properties, reactions, occurrences and uses* (pp. 365–407). Weinheim: Wiley-VCH Verlag GmbH & Co. KGaA. <https://doi.org/10.1002/3527602097.ch14>
- Cornwell, J. C., & Morse, J. W. (1987). The characterization of iron sulfide minerals in anoxic marine sediments. *Marine Chemistry*, 22(2–4), 193–206. [https://doi.org/10.1016/0304-4203\(87\)90008-9](https://doi.org/10.1016/0304-4203(87)90008-9)
- Costa Pisani, P., Reshet, M., & Moore, G. (2005). Targeted 3-D prestack depth imaging at Legs 190–196 ODP drill sites (Nankai Trough, Japan). *Geophysical Research Letters*, 32(20), L20309. <https://doi.org/10.1029/2005GL024191>
- DeMets, C., Gordon, R. G., & Argus, D. F. (2010). Geologically current plate motions. *Geophysical Journal International*, 181(1), 1–80. <https://doi.org/10.1111/j.1365-246X.2009.04491.x>

- D'Hondt, S., Inagaki, F., Zarikian, C. A., Abrams, L. J., Dubois, N., Engelhardt, T., et al. (2015). Presence of oxygen and anaerobic communities from sea floor to basement in deep-sea sediments. *Nature Geoscience*, 8(4), 299–304. <https://doi.org/10.1038/ngeo2387>
- D'Hondt, S., Rutherford, S., & Spivack, A. J. (2002). Metabolic activity of subsurface life in deep-sea sediments. *Science*, 295(5562), 2067–2070. <https://doi.org/10.1126/science.1064878>
- Dymond, J., Suess, E., & Lyle, M. (1992). Barium in deep-sea sediment: A geochemical proxy for paleoproductivity. *Paleoceanography*, 7(2), 163–181. <https://doi.org/10.1029/92PA00181>
- Emerson, S., Jahnke, R., Bender, M., Froelich, P., Klinkhammer, G., Bowser, C., & Setlock, G. (1980). Early diagenesis in sediments from the eastern equatorial Pacific, I. Pore water nutrient and carbonate results. *Earth and Planetary Science Letters*, 49(1), 57–80. [https://doi.org/10.1016/0012-821X\(80\)90150-8](https://doi.org/10.1016/0012-821X(80)90150-8)
- Fischer, D., Mogollón, J. M., Strasser, M., Pape, T., Bohrmann, G., Fekete, N., et al. (2013). Subduction zone earthquake as potential trigger of submarine hydrocarbon seepage. *Nature Geoscience*, 6(8), 647–651. <https://doi.org/10.1038/ngeo1886>
- Froelich, P. N., Klinkhammer, G. P., Bender, M. L., Luedtke, N. A., Heath, G. R., Cullen, D., et al. (1979). Early oxidation of organic matter in pelagic sediments of the eastern equatorial Atlantic: Suboxic diagenesis. *Geochimica et Cosmochimica Acta*, 43(7), 1075–1090. [https://doi.org/10.1016/0016-7037\(79\)90095-4](https://doi.org/10.1016/0016-7037(79)90095-4)
- Fu, Y., von Döbenek, T., Franke, C., Heslop, D., & Kasten, S. (2008). Rock magnetic identification and geochemical process models of greigite formation in Quaternary marine sediments from the Gulf of Mexico (IODP Hole U1319A). *Earth and Planetary Science Letters*, 275, 233–245. <https://doi.org/10.1016/j.epsl.2008.07.034>
- Funk, J. A., von Döbenek, T., & Reitz, A. (2004). Integrated rock magnetic and geochemical quantification of redoxomorphic iron mineral diagenesis in Late Quaternary sediments from the Equatorial Atlantic. In G. Wefer, S. Mulitza, & V. Rattmeyer (Eds.), *The South Atlantic in the Late Quaternary* (pp. 61–101). Berlin, Heidelberg: Springer. [https://doi.org/10.1007/978-3-642-18917-3\\_12](https://doi.org/10.1007/978-3-642-18917-3_12)
- Goldhaber, M. B., & Kaplan, I. R. (1974). The sulfur cycle. In E. D. Goldberg (Ed.), *The Sea* (Vol. 5, pp. 569–655). New York, NY: Wiley-Interscience.
- Guo, Y. J. (1991). The Kuroshio, Part II. Primary production and phytoplankton. *Oceanography and Marine Biology*, 29, 155–189.
- Hagino, K., & the Expedition 370 Scientists. (2018). Data report: Calcareous nannofossils from the middle Miocene to Pleistocene, IODP Expedition 370 Site C0023. In V. B. Heuer, F. Inagaki, Y. Morono, Y. Kubo, & L. Maeda (Eds.), *Proceedings of the International Ocean Discovery Program*. (Vol. 370). College Station, TX: International Ocean Discovery Program. <https://doi.org/10.14379/iodp.proc.370.201.2018>
- Harris, R., Yamano, M., Kinoshita, M., Spinelli, G., Hamamoto, H., & Ashi, J. (2013). A synthesis of heat flow determinations and thermal modeling along the Nankai Trough, Japan. *Journal of Geophysical Research: Solid Earth*, 118(6), 2687–2702. <https://doi.org/10.1002/jgrb.50230>
- Henkel, S., Kasten, S., Hartmann, J. F., Silva-Busso, A., & Staubwasser, M. (2018). Iron cycling and stable Fe isotope fractionation in Antarctic shelf sediments, King George Island. *Geochimica et Cosmochimica Acta*, 237, 320–338. <https://doi.org/10.1016/j.gca.2018.06.042>
- Henkel, S., Kasten, S., Poulton, S. W., & Staubwasser, M. (2016). Determination of the stable iron isotopic composition of sequentially leached iron phases in marine sediments. *Chemical Geology*, 421, 93–102. <https://doi.org/10.1016/j.chemgeo.2015.12.003>
- Henkel, S., Mogollón, J. M., Nöthen, K., Franke, C., Bogus, K., Robin, E., et al. (2012). Diagenetic barium cycling in Black Sea sediments—A case study for anoxic marine environments. *Geochimica et Cosmochimica Acta*, 88, 88–105. <https://doi.org/10.1016/j.gca.2012.04.021>
- Hensen, C., Zabel, M., Pfeifer, K., Schwenk, T., Kasten, S., Riedinger, N., et al. (2003). Control of sulfate pore-water profiles by sedimentary events and the significance of anaerobic oxidation of methane for the burial of sulfur in marine sediments. *Geochimica et Cosmochimica Acta*, 67(14), 2631–2647. [https://doi.org/10.1016/S0016-7037\(03\)00199-6](https://doi.org/10.1016/S0016-7037(03)00199-6)
- Hepburn, L. E., Butler, I. B., Boyce, A., & Schröder, C. (2020). The use of operationally-defined sequential Fe extraction methods for mineralogical applications: A cautionary tale from Mössbauer spectroscopy. *Chemical Geology*, 543, 119584. <https://doi.org/10.1016/j.chemgeo.2020.119584>
- Heron, G., Crouzet, C., Bourg, A. C., & Christensen, T. H. (1994). Speciation of Fe (II) and Fe (III) in contaminated aquifer sediments using chemical extraction techniques. *Environmental Science & Technology*, 28(9), 1698–1705. <https://doi.org/10.1021/es00058a023>
- Heslop, D., Dekkers, M. J., Kruiver, P. P., & van Oorschot, I. H. M. (2002). Analysis of isothermal remanent magnetization acquisition curves using expectation-maximization algorithm. *Geophysical Journal International*, 148(1), 58–64. <https://doi.org/10.1046/j.0956-540x.2001.01558.x>
- Heuer, V. B., Inagaki, F., Morono, Y., Kubo, Y., Maeda, L., & the Expedition 370 Scientists (2017a). Temperature limit of the deep biosphere off Muroto. *Proceedings of the International Ocean Discovery Program* (Vol. 370). College Station, TX: International Ocean Discovery Program. <https://doi.org/10.14379/iodp.proc.370.2017>
- Heuer, V. B., Inagaki, F., Morono, Y., Kubo, Y., Maeda, L., & the Expedition 370 Scientists (2017b). Site C0023. In V. B. Heuer, F. Inagaki, Y. Morono, Y. Kubo, & L. Maeda (Eds.), *Proceedings of the International Ocean Discovery Program* (Vol. 370). College Station, TX: International Ocean Discovery Program. <https://doi.org/10.14379/iodp.proc.370.103.2017>
- Heuer, V. B., Inagaki, F., Morono, Y., Kubo, Y., Spivack, A., Viehweger, B., et al. (2020). Temperature limits to deep seafloor life in the Nankai Trough subduction zone. *Science*, 370(6521), 1230–1234. <https://doi.org/10.1126/science.abd7934>
- Hirota, Y. (1995). The Kuroshio, Part III. Zooplankton. *Oceanography and Marine Biology*, 33, 151–220.
- Holler, T., Widdel, F., Knittel, K., Amann, R., Kellermann, M. Y., Hinrichs, K.-U., et al. (2011). Thermophilic anaerobic oxidation of methane by marine microbial consortia. *The ISME Journal*, 5(12), 1946–1956. <https://doi.org/10.1038/ismej.2011.77>
- Horsfield, B., Schenk, H. J., Zink, K., Ondrak, R., Dieckmann, V., Kallmeyer, J., et al. (2006). Living microbial ecosystems within the active zone of catagenesis: Implications for feeding the deep biosphere. *Earth and Planetary Science Letters*, 246(1–2), 55–69. <https://doi.org/10.1016/j.epsl.2006.03.040>
- Ijiri, A., Inagaki, F., Kubo, Y., Adhikari, R. R., Hattori, S., Hoshino, T., et al. (2018). Deep-biosphere methane production stimulated by geofluids in the Nankai accretionary complex. *Science Advances*, 4(6), eaao4631. <https://doi.org/10.1126/sciadv.aao4631>
- Ike, T., Moore, G. F., Kuramoto, S., Park, J.-O., Kaneda, Y., & Taira, A. (2008). Tectonics and sedimentation around Kashinosaki Knoll: A subducting basement high in the eastern Nankai Trough. *Island Arc*, 17(3), 358–375. <https://doi.org/10.1111/j.1440-1738.2008.00625.x>
- Inagaki, F., Hinrichs, K.-U., Kubo, Y., Bowles, M. W., Heuer, V. B., Hong, W.-L., et al. (2015). Exploring deep microbial life in coal-bearing sediment down to ~2.5 km below the ocean floor. *Science*, 349(6246), 420–424. <https://doi.org/10.1126/science.aaa6882>
- Jørgensen, B. B. (1982). Mineralization of organic matter in the sea bed—The role of sulphate reduction. *Nature*, 296(5858), 643–645. <https://doi.org/10.1038/296643a0>
- Jørgensen, B. B., Böttcher, M. E., Lüschen, H., Neretin, L. N., & Volkov, I. I. (2004). Anaerobic methane oxidation and a deep H<sub>2</sub>S sink generate isotopically heavy sulfides in Black Sea sediments. *Geochimica et Cosmochimica Acta*, 68(9), 2095–2118. <https://doi.org/10.1016/j.gca.2003.07.017>

- Jørgensen, B. B., Findlay, A. J., & Pellerin, A. (2019). The biogeochemical sulfur cycle of marine sediment. *Frontiers in Microbiology*, *10*, 849. <https://doi.org/10.3389/fmicb.2019.00849>
- Jørgensen, B. B., & Kasten, S. (2006). Sulfur cycling and methane oxidation. In H. D. Schulz, & M. Zabel (Eds.), *Marine Geochemistry* (pp. 271–309). Berlin, Heidelberg: Springer. [https://doi.org/10.1007/3-540-32144-6\\_8](https://doi.org/10.1007/3-540-32144-6_8)
- Jung, J., Yoo, K.-C., Rosenheim, B. E., Conway, T. M., Lee, J. I., Yoon, H. I., et al. (2019). Microbial Fe(III) reduction as a potential iron source from Holocene sediments beneath Larsen Ice Shelf. *Nature Communications*, *10*(1), 1–10. <https://doi.org/10.1038/s41467-019-13741-x>
- Kamata, H., & Kodama, K. (1994). Tectonics of an arc-arc junction: An example from Kyushu Island at the junction of the Southwest Japan Arc and the Ryukyu Arc. *Tectonophysics*, *233*(1–2), 69–81. [https://doi.org/10.1016/0040-1951\(94\)90220-8](https://doi.org/10.1016/0040-1951(94)90220-8)
- Kars, M., & Köster, M. (2021). Rock magnetic data of IODP Hole 370-C0023A. *PANGAEA*, <https://doi.pangaea.de/10.1594/PANGAEA.929380>
- Kashefi, K., & Lovley, D. R. (2003). Extending the upper temperature limit for life. *Science*, *301*(5635), 934. <https://doi.org/10.1126/science.1086823>
- Kasten, S., Freudenthal, T., Gingele, F. X., & Schulz, H. D. (1998). Simultaneous formation of iron-rich layers at different redox boundaries in sediments of the Amazon deep-sea fan. *Geochimica et Cosmochimica Acta*, *62*(13), 2253–2264. [https://doi.org/10.1016/S0016-7037\(98\)00093-3](https://doi.org/10.1016/S0016-7037(98)00093-3)
- Kasten, S., Zabel, M., Heuer, V., & Hensen, C. (2003). Processes and signals of nonsteady-state diagenesis in deep-sea sediments and their pore waters. In G. Wefer, S. Mulitza, & V. Rattmeyer (Eds.), *The South Atlantic in the Late Quaternary* (pp. 431–459). Berlin, Heidelberg: Springer. [https://doi.org/10.1007/978-3-642-18917-3\\_20](https://doi.org/10.1007/978-3-642-18917-3_20)
- Kim, J., Dong, H., Seabaugh, J., Newell, S. W., & Eberl, D. D. (2004). Role of microbes in the smectite-to-illite reaction. *Science*, *303*(5659), 830–832. <https://doi.org/10.1126/science.1093245>
- Kim, J., Dong, H., Yang, K., Park, H., Elliott, W. C., Spivack, A., et al. (2019). Naturally occurring, microbially induced smectite-to-illite reaction. *Geology*, *47*(6), 535–539. <https://doi.org/10.1130/G46122.1>
- Korff, L., von Dobeneck, T., Frederichs, T., Kasten, S., Kuhn, G., Gersonde, R., & Diekmann, B. (2016). Cyclic magnetite dissolution in Pleistocene sediments of the abyssal northwest Pacific Ocean: Evidence for glacial oxygen depletion and carbon trapping. *Paleoceanography*, *31*(5), 600–624. <https://doi.org/10.1002/2015PA002882>
- Köster, M., Kars, M., Schubotz, F., Tsang, M.-Y., Maisch, M., Kappler, A., et al. (2021a). Solid-phase geochemistry of sediment cores from IODP Hole 370-C0023A. *PANGAEA*. <https://doi.org/10.1594/PANGAEA.930858>
- Köster, M., Kars, M., Schubotz, F., Tsang, M.-Y., Maisch, M., Kappler, A., et al. (2021b). Rock magnetic end-member unmixing of sediment cores from IODP Hole 370-C0023A. *PANGAEA*. <https://doi.org/10.1594/PANGAEA.929317>
- Kruiver, P. P., Dekkers, M. J., & Heslop, D. (2001). Quantification of magnetic coercivity components by the analysis of acquisition curves of isothermal remanent magnetisation. *Earth and Planetary Science Letters*, *189*(3–4), 269–276. [https://doi.org/10.1016/S0012-821X\(01\)00367-3](https://doi.org/10.1016/S0012-821X(01)00367-3)
- Kuhnt, W., Holbourn, A., Hall, R., Zuvela, M., & Käse, R. (2004). Neogene history of the Indonesian throughflow. In P. Clift, W. Kuhnt, P. Wang, & D. Hayes (Eds.), *Continent-ocean interactions within East Asian marginal seas. Geophysical Monograph Series 149* (pp. 299–320). Washington, DC: American Geophysical Union. <https://doi.org/10.1029/149gm16>
- Laufer, K., Michaud, A. B., Røy, H., & Jørgensen, B. B. (2020). Reactivity of iron minerals in the seabed toward microbial reduction—A comparison of different extraction techniques. *Geomicrobiology Journal*, *37*(2), 170–189. <https://doi.org/10.1080/01490451.2019.1679291>
- Lawrence, K. T., Sigman, D. M., Herbert, T. D., Riihimäki, C. A., Bolton, C. T., Martínez-García, A., et al. (2013). Time-transgressive North Atlantic productivity changes upon Northern Hemisphere glaciation. *Paleoceanography*, *28*(4), 740–751. <https://doi.org/10.1002/2013PA002546>
- LePichon, X., Iiyama, T., Boulègue, J., Charvet, J., Faure, M., Kano, K., et al. (1987). Nankai Trough and Zenisu Ridge: A deep-sea submersible survey. *Earth and Planetary Science Letters*, *83*(1–4), 285–299. [https://doi.org/10.1016/0012-821X\(87\)90072-0](https://doi.org/10.1016/0012-821X(87)90072-0)
- Mahony, S. H., Wallace, L. M., Miyoshi, M., Villamor, P., Sparks, R. S. J., & Hasenaka, T. (2011). Volcano-tectonic interactions during rapid plate-boundary evolution in the Kyushu region, SW Japan. *GSA Bulletin*, *123*(11–12), 2201–2223. <https://doi.org/10.1130/B30408.1>
- Manheim, F. T., & Sayles, F. L. (1974). Composition and origin of interstitial waters of marine sediments, based on deep sea drill cores. In E. D. Goldberg (Ed.), *The Sea (Volume 5): Marine chemistry: The sedimentary cycle* (pp. 527–568). New York, NY: Wiley-Interscience.
- März, C., Hoffmann, J., Bleil, U., de Lange, G. J., & Kasten, S. (2008). Diagenetic changes of magnetic and geochemical signals by anaerobic methane oxidation in sediments of the Zambezi deep-sea fan (SW Indian Ocean). *Marine Geology*, *255*(3–4), 118–130. <https://doi.org/10.1016/j.margeo.2008.05.013>
- Maxbauer, D. P., Feinberg, J. M., & Fox, D. L. (2016). MAX UnMix: A web application for unmixing magnetic coercivity distributions. *Computers & Geosciences*, *95*, 140–145. <https://doi.org/10.1016/j.cageo.2016.07.009>
- Meister, P. (2015). For the deep biosphere, the present is not always the key to the past: What we can learn from the geological record. *Terra Nova*, *27*(6), 400–408. <https://doi.org/10.1111/ter.12174>
- Mewes, K., Mogollón, J. M., Picard, A., Rühlemann, C., Kuhn, T., Nöthen, K., & Kasten, S. (2014). Impact of depositional and biogeochemical processes on small scale variations in nodule abundance in the Clarion-Clipperton fracture zone. *Deep Sea Research Part I: Oceanographic Research Papers*, *91*, 125–141. <https://doi.org/10.1016/j.dsr.2014.06.001>
- Meyers, P. A. (1994). Preservation of elemental and isotopic source identification of sedimentary organic matter. *Chemical Geology*, *114*(3–4), 289–302. [https://doi.org/10.1016/0009-2541\(94\)90059-0](https://doi.org/10.1016/0009-2541(94)90059-0)
- Meyers, P. A. (1997). Organic geochemical proxies of paleoceanographic, paleolimnologic, and paleoclimatic processes. *Organic Geochemistry*, *27*(5–6), 213–250. [https://doi.org/10.1016/S0146-6380\(97\)00049-1](https://doi.org/10.1016/S0146-6380(97)00049-1)
- Mizutani, H., & Wada, E. (1982). Effect of high atmospheric CO<sub>2</sub> concentration on δ<sup>13</sup> of algae. *Origins of Life*, *12*(4), 377–390. <https://doi.org/10.1007/BF00927070>
- Mogollón, J. M., Mewes, K., & Kasten, S. (2016). Quantifying manganese and nitrogen cycle coupling in manganese-rich, organic carbon-starved marine sediments: Examples from the Clarion-Clipperton fracture zone. *Geophysical Research Letters*, *43*(13), 7114–7123. <https://doi.org/10.1002/2016GL069117>
- Molina-Cruz, A. (1997). Closing of the Central American Gateway and its effect on the distribution of late Pliocene radiolarians in the eastern tropical Pacific. *Tectonophysics*, *281*(1–2), 105–111. [https://doi.org/10.1016/S0040-1951\(97\)00162-5](https://doi.org/10.1016/S0040-1951(97)00162-5)
- Morono, Y., Inagaki, F., Heuer, V. B., Kubo, Y., Maeda, L., & the Expedition 370 Scientists (2017). Expedition 370 methods. In V. B. Heuer, F. Inagaki, Y. Morono, Y. Kubo, & L. Maeda (Eds.), *Proceedings of the International Ocean Discovery Program* (Vol. 370). College Station, TX: International Ocean Discovery Program. <https://doi.org/10.14379/iodp.proc.370.102.2017>



- Murad, E. (1998). Clays and clay minerals: What can Mössbauer spectroscopy do to help understand them? *Hyperfine Interactions*, 117(1–4), 39–70. <https://doi.org/10.1023/A:1012635124874>
- Murad, E. (2010). Mössbauer spectroscopy of clays, soils and their mineral constituents. *Clay Minerals*, 45(1), 413–430. <https://doi.org/10.1180/claymin.2010.045.4.413>
- Niewöhner, C., Hensen, C., Kasten, S., Zabel, M., & Schulz, H. D. (1998). Deep sulfate reduction completely mediated by anaerobic methane oxidation in sediments of the upwelling area off Namibia. *Geochimica et Cosmochimica Acta*, 62(3), 455–464. [https://doi.org/10.1016/S0016-7037\(98\)00055-6](https://doi.org/10.1016/S0016-7037(98)00055-6)
- Nöthen, K., & Kasten, S. (2011). Reconstructing changes in seep activity by means of pore water and solid phase Sr/Ca and Mg/Ca ratios in pockmark sediments of the Northern Congo Fan. *Marine Geology*, 287(1–4), 1–13. <https://doi.org/10.1016/j.margeo.2011.06.008>
- Okino, K., Ohara, Y., Kasuga, S., & Kato, Y. (1999). The Philippine Sea: New survey results reveal the structure and the history of the marginal basins. *Geophysical Research Letters*, 26(15), 2287–2290. <https://doi.org/10.1029/1999GL900537>
- Okino, K., Shimakawa, Y., & Nagaoka, S. (1994). Evolution of the Shikoku basin. *Journal of Geomagnetism and Geoelectricity*, 46(6), 463–479. <https://doi.org/10.5636/jgg.46.463>
- Oonk, P. B., Tsikos, H., Mason, P. R., Henkel, S., Staubwasser, M., Fryer, L., et al. (2017). Fraction-specific controls on the trace element distribution in iron formations: Implications for trace metal stable isotope proxies. *Chemical Geology*, 474, 17–32. <https://doi.org/10.1016/j.chemgeo.2017.10.018>
- Parkes, R. J., Wellsbury, P., Mather, I. D., Cobb, S. J., Cragg, B. A., Hornibrook, E. R. C., & Horsfield, B. (2007). Temperature activation of organic matter and minerals during burial has the potential to sustain the deep biosphere over geological timescales. *Organic Geochemistry*, 38(6), 845–852. <https://doi.org/10.1016/j.orggeochem.2006.12.011>
- Passier, H. F., Middelburg, J. J., van Os, B. J. H., & de Lange, G. J. (1996). Diagenetic pyritisation under eastern Mediterranean sapropels caused by downward sulphide diffusion. *Geochimica et Cosmochimica Acta*, 60(5), 751–763. [https://doi.org/10.1016/0016-7037\(95\)00419-X](https://doi.org/10.1016/0016-7037(95)00419-X)
- Pickering, K. T., Underwood, M. B., Saito, S., Naruse, H., Kutterolf, S., Scudder, R., et al. (2013). Depositional architecture, provenance, and tectonic/eustatic modulation of Miocene submarine fans in the Shikoku basin: Results from Nankai Trough seismogenic zone experiment. *Geochemistry, Geophysics, Geosystems*, 14(6), 1722–1739. <https://doi.org/10.1002/ggge.20107>
- Poulton, S. W., & Canfield, D. E. (2005). Development of a sequential extraction procedure for iron: Implications for iron partitioning in continentally derived particulates. *Chemical Geology*, 214(3–4), 209–221. <https://doi.org/10.1016/j.chemgeo.2004.09.003>
- Poulton, S. W., Krom, M. D., & Raiswell, R. (2004). A revised scheme for the reactivity of iron (oxyhydr) oxide minerals towards dissolved sulfide. *Geochimica et Cosmochimica Acta*, 68(18), 3703–3715. <https://doi.org/10.1016/j.gca.2004.03.012>
- Pruyvers, P. A., de Lange, G. J., Middelburg, J. J., & Hydes, D. J. (1993). The diagenetic formation of metal-rich layers in sapropel-containing sediments in the eastern Mediterranean. *Geochimica et Cosmochimica Acta*, 57(3), 527–536. [https://doi.org/10.1016/0016-7037\(93\)90365-4](https://doi.org/10.1016/0016-7037(93)90365-4)
- Qui, B. (2001). Kuroshio and Oyashio currents. In K. K. Turekian, J. H. Steele, & S. A. Thorpe (Eds.), *Encyclopedia of ocean sciences* (pp. 1413–1425). Cambridge, MA: Academic Press. <https://doi.org/10.1006/rwos.2001.0350>
- Riedinger, N., Formolo, M. J., Lyons, T. W., Henkel, S., Beck, A., & Kasten, S. (2014). An inorganic geochemical argument for coupled anaerobic oxidation of methane and iron reduction in marine sediments. *Geobiology*, 12(2), 172–181. <https://doi.org/10.1111/gbi.12077>
- Riedinger, N., Kasten, S., Gröger, J., Franke, C., & Pfeifer, K. (2006). Active and buried authigenic barite fronts in sediments from the Eastern Cape basin. *Earth and Planetary Science Letters*, 241(3–4), 876–887. <https://doi.org/10.1016/j.epsl.2005.10.032>
- Riedinger, N., Pfeifer, K., Kasten, S., Garming, J. F. L., Vogt, C., & Hensen, C. (2005). Diagenetic alteration of magnetic signals by anaerobic oxidation of methane related to a change in sedimentation rate. *Geochimica et Cosmochimica Acta*, 69(16), 4117–4126. <https://doi.org/10.1016/j.gca.2005.02.004>
- Riedinger, N., Strasser, M., Harris, R. N., Klockgether, G., Lyons, T. W., & Srean, E. J. (2015). Deep subsurface carbon cycling in the Nankai Trough (Japan)—Evidence of tectonically induced stimulation of a deep microbial biosphere. *Geochemistry, Geophysics, Geosystems*, 16(9), 3257–3270. <https://doi.org/10.1002/2015GC006050>
- Roberts, A. P. (2015). Magnetic mineral diagenesis. *Earth-Science Reviews*, 151, 1–47. <https://doi.org/10.1016/j.earscirev.2015.09.010>
- Roberts, A. P., Chang, L., Rowan, C. J., Horng, C. S., & Florindo, F. (2011). Magnetic properties of sedimentary greigite (Fe<sub>3</sub>S<sub>4</sub>): An update. *Reviews of Geophysics*, 49(1), RG1002. <https://doi.org/10.1029/2010RG000336>
- Robertson, D. J., & France, D. E. (1994). Discrimination of remanence-carrying minerals in mixtures, using isothermal remanent magnetization acquisition curves. *Physics of the Earth and Planetary Interiors*, 82(3–4), 223–234. [https://doi.org/10.1016/0031-9201\(94\)90074-4](https://doi.org/10.1016/0031-9201(94)90074-4)
- Ryan, P. C., Hillier, S., & Wall, J. (2008). Stepwise effects of the BCR sequential chemical extraction procedure on dissolution and metal release from common ferromagnesian clay minerals: A combined solution chemistry and X-ray powder diffraction study. *The Science of the Total Environment*, 407(1), 603–614. <https://doi.org/10.1016/j.scitotenv.2008.09.019>
- Saitoh, Y., Ishikawa, T., Tanimizu, M., Murayama, M., Ujiie, Y., Yamamoto, Y., et al. (2015). Sr, Nd, and Pb isotope compositions of hemipelagic sediment in the Shikoku Basin: Implications for sediment transport by the Kuroshio and Philippine Sea plate motion in the late Cenozoic. *Earth and Planetary Science Letters*, 421, 47–57. <https://doi.org/10.1016/j.epsl.2015.04.001>
- Seno, T., Stein, S., & Gripp, A. E. (1993). A model for the notion of the Philippine Sea Plate consistent with NUVEL-1 and geological data. *Journal of Geophysical Research*, 98(B10), 17941–17948. <https://doi.org/10.1029/93JB00782>
- Shi, M., Wu, H., Roberts, A. P., Zhang, S., Zhao, X., Li, H., et al. (2017). Tectonic, climatic, and diagenetic control of magnetic properties of sediments from Kumano basin, Nankai margin, southwestern Japan. *Marine Geology*, 391, 1–12. <https://doi.org/10.1016/j.margeo.2017.07.006>
- Shipboard Science Party. (1991). Site 808. In A. Taira, I. Hill, J. V. Firth, et al. (Eds.), *Proceedings of the ocean drilling program, Initial Reports*, 131 (pp. 71–269). College Station, TX: Ocean Drilling Program. <https://doi.org/10.2973/odp.proc.ir.131.106.1991>
- Shipboard Science Party. (2001). Site 1174. In G. F. Moore, A. Taira, A. Klaus, et al. (Eds.), *Proceedings of the ocean drilling program, Initial Reports*, 190 (pp. 1–149). College Station, TX: Ocean Drilling Program. <https://doi.org/10.2973/odp.proc.ir.190.105.2001>
- Slotznick, S. P., Sperling, E. A., Tosca, N. J., Miller, A. J., Clayton, K. E., van Helmond, N. A. G. M., et al. (2020). Unraveling the mineralogy complexity of sediment iron speciation using sequential extractions. *Geochemistry, Geophysics, Geosystems*, 21(2), E2019GC008666. <https://doi.org/10.1029/2019GC008666>
- Stokey, L. L. (1970). Ferrozine—A new spectrophotometric reagent for iron. *Analytical Chemistry*, 42(7), 779–781. <https://doi.org/10.1021/ac60289a016>
- Stucki, J. W., Bailey, G. W., & Gan, H. M. (1996). Oxidation-reduction mechanisms in iron-bearing phyllosilicates. *Applied Clay Science*, 10(6), 417–430. [https://doi.org/10.1016/0169-1317\(96\)00002-6](https://doi.org/10.1016/0169-1317(96)00002-6)
- Stucki, J. W., Golden, D. C., & Roth, C. B. (1984). Effects of reduction and reoxidation of structural iron on the surface charge and dissolution of dioctahedral smectites. *Clays and Clay Minerals*, 32(5), 350–356. <https://doi.org/10.1346/CCMN.1984.0320502>

- Sturt, H. F., Summons, R. E., Smith, K., Elvert, M., & Hinrichs, K.-U. (2004). Intact polar membrane lipids in prokaryotes and sediments deciphered by high-performance liquid chromatography/electrospray ionization multistage mass spectrometry—New biomarkers for biogeochemistry and microbial ecology. *Rapid Communications in Mass Spectrometry*, 18(6), 617–628. <https://doi.org/10.1002/rcm.1378>
- Swann, G. E., Maslin, M. A., Leng, M. J., Sloane, H. J., & Haug, G. H. (2006). Diatom  $\delta^{18}\text{O}$  evidence for the development of the modern halocline system in the subarctic northwest Pacific at the onset of major Northern Hemisphere glaciation. *Paleoceanography*, 21(1), PA1009. <https://doi.org/10.1029/2005PA001147>
- Sweeney, R. E., & Kaplan, I. R. (1973). Pyrite framboid formation: Laboratory synthesis and marine sediments. *Economic Geology*, 68(5), 618–634. <https://doi.org/10.2113/gsecongeo.68.5.618>
- Taira, A., & Ashi, J. (1993). Sedimentary facies evolution of the Nankai forearc and its implications for the growth of the Shimanto accretionary prism. In I. A. Hill, A. Taira, J. V. Firth, et al. (Eds.), *Proceedings of the ocean drilling program Initial Reports*, 131 (pp. 331–341). College Station, TX: Ocean Drilling Program. <https://doi.org/10.2973/odp.proc.sr.131.136.1993>
- Taira, A., Hill, I., Firth, J., Berner, U., Brückmann, W., Byrne, T., et al. (1992). Sediment deformation and hydrogeology of the Nankai Trough accretionary prism: Synthesis of shipboard results of ODP Leg 131. *Earth and Planetary Science Letters*, 109(3–4), 431–450. [https://doi.org/10.1016/0012-821x\(92\)90104-4](https://doi.org/10.1016/0012-821x(92)90104-4)
- Tessier, A., Campbell, P. G., & Bisson, M. (1979). Sequential extraction procedure for the speciation of particulate trace metals. *Analytical Chemistry*, 51(7), 844–851. <https://doi.org/10.1021/ac50043a017>
- Thompson, R., Stober, J. C., Turner, G. M., Oldfield, F., Bloemendal, J., Dearing, J. A., & Rummery, T. A. (1980). Environmental applications of magnetic measurements. *Science*, 207(4430), 481–486. <https://doi.org/10.1126/science.207.4430.481>
- Torres, M. E., Cox, T., Hong, W.-L., McManus, J., Sample, J. C., Desfrigneville, C., et al. (2015). Crustal fluid and ash alteration impacts on the biosphere of Shikoku basin sediments, Nankai Trough, Japan. *Geobiology*, 13(6), 562–580. <https://doi.org/10.1111/gbi.12146>
- Tsang, M. Y., Bowden, S. A., Wang, Z., Mohammed, A., Tonai, S., Muirhead, D., et al. (2020). Hot fluids, burial metamorphism and thermal histories in the underthrust sediments at IODP 370 site C0023, Nankai accretionary complex. *Marine and Petroleum Geology*, 112, 104080. <https://doi.org/10.1016/j.marpetgeo.2019.104080>
- Tsuchi, R. (1997). Marine climatic responses to Neogene tectonics to the Pacific Ocean seaways. *Tectonophysics*, 281(1–2), 113–124. [https://doi.org/10.1016/S0040-1951\(97\)00163-7](https://doi.org/10.1016/S0040-1951(97)00163-7)
- Turekian, K. K., & Wedepohl, K. H. (1961). Distribution of the elements in some major units of the Earth's crust. *The Geological Society of America Bulletin*, 72(2), 175–192. [https://doi.org/10.1130/0016-7606\(1961\)72\[175:DOTEIS\]2.0.CO;2](https://doi.org/10.1130/0016-7606(1961)72[175:DOTEIS]2.0.CO;2)
- Underwood, M. B., & Guo, J. (2018). Clay-mineral assemblages across the Nankai-Shikoku subduction system, offshore Japan: A synthesis of results from the NanTroSEIZE project. *Geosphere*, 14(5), 2009–2043. <https://doi.org/10.1130/GES01626.1>
- Underwood, M. B., Saito, S., & Kubo, Y. (2010). IODP Expedition 322 drills two sites to document inputs to the Nankai Trough subduction zone. *Scientific Drilling*, 10, 14–25. <https://doi.org/10.2204/iodp.sd.10.02.21010.5194/sd-10-14-2010>
- Underwood, M. B., & Steurer, J. F. (2003). Composition and sources of clay from the trench slope and shallow accretionary prism of Nankai Trough. In H. Mikada, G. F. Moore, A. Taira, K. Becker, J. C. Moore, & A. Klaus (Eds.), *Proceedings of the Ocean drilling program, scientific results* (Vol. 190/196, pp. 1–28). College Station, TX: Ocean Drilling Program. <https://doi.org/10.2973/odp.proc.sr.190196.206.2003>
- Vargas, M., Kashefi, K., Blunt-Harris, E. L., & Lovley, D. R. (1998). Microbiological evidence for Fe (III) reduction on early Earth. *Nature*, 395(6697), 65–67. <https://doi.org/10.1038/25720>
- Volkman, J. K., Barrett, S. M., Dunstan, G. A., & Jeffrey, S. W. (1992). C<sub>30</sub>-C<sub>32</sub> alkyl diols and unsaturated alcohols in microalgae of the class Eustigmatophyceae. *Organic Geochemistry*, 18(1), 131–138. [https://doi.org/10.1016/0146-6380\(92\)90150-V](https://doi.org/10.1016/0146-6380(92)90150-V)
- Volz, J. B., Mogollón, J. M., Geibert, W., Martínez Arbizu, P., Koschinsky, A., & Kasten, S. (2018). Natural spatial variability of depositional conditions, biogeochemical processes and element fluxes in sediments of the eastern Clarion-Clipperton Zone, Pacific Ocean. *Deep Sea Research Part I: Oceanographic Research Papers*, 140, 159–172. <https://doi.org/10.1016/j.dsr.2018.08.006>
- Vorhies, J. S., & Gaines, R. R. (2009). Microbial dissolution of clay minerals as a source of iron and silica in marine sediments. *Nature Geoscience*, 2(3), 221–225. <https://doi.org/10.1038/ngeo441>
- Watts, A. B., & Weissel, J. K. (1975). Tectonic history of the Shikoku marginal basin. *Earth and Planetary Science Letters*, 25(3), 239–250. [https://doi.org/10.1016/0012-821X\(75\)90238-1](https://doi.org/10.1016/0012-821X(75)90238-1)
- Wehrmann, L. M., Arndt, S., März, C., Ferdelman, T. G., & Brunner, B. (2013). The evolution of early diagenetic signals in Bering Sea subseafloor sediments in response to varying organic carbon deposition over the last 4.3 Ma. *Geochimica et Cosmochimica Acta*, 109, 175–196. <https://doi.org/10.1016/j.gca.2013.01.025>
- Wehrmann, L. M., & Riedinger, N. (2016). The sedimentary deep subseafloor biosphere. In J. K. Cochran, H. J. Bokuniewicz, & P. L. Yager (Eds.), *Encyclopedia of Ocean Sciences* (3rd ed., pp. 258–274). Academic Press. <https://doi.org/10.1016/B978-0-12-409548-9.09741-4>
- Wellsbury, P., Goodman, K., Barth, T., Cragg, B. A., Barnes, S. P., & Parkes, R. J. (1997). Deep marine biosphere fueled by increasing organic matter availability during burial and heating. *Nature*, 388, 573–576. <https://doi.org/10.1038/41544>
- Wilkin, R. T., & Barnes, H. L. (1996). Pyrite formation by reactions of iron monosulfides with dissolved inorganic and organic sulfur species. *Geochimica et Cosmochimica Acta*, 60(21), 4167–4179. [https://doi.org/10.1016/S0016-7037\(97\)81466-4](https://doi.org/10.1016/S0016-7037(97)81466-4)
- Yamano, M., Kinoshita, M., Goto, S., & Matsubayashi, O. (1992). Extremely high heat flow anomaly in the middle part of the Nankai Trough. *Physics and Chemistry of the Earth, Parts A/B/C*, 28(9–11), 487–497. [https://doi.org/10.1016/S1474-7065\(03\)00068-8](https://doi.org/10.1016/S1474-7065(03)00068-8)
- Zhabina, N. N., & Volkov, I. I. (1978). A method of determination of various sulfur compounds in sea sediments and rocks. In W. E. Krumbein (Ed.), *Environmental biogeochemistry and geomicrobiology: methods, metals and assessment* (Vol. 3, pp. 735–745). Michigan: Ann Arbor Scientific Publications.
- Zonneveld, K. A. F., Versteegh, G. J. M., Kasten, S., Eglinton, T. I., Emeis, K.-C., Huguet, C., et al. (2010). Selective preservation of organic matter in marine environments; processes and impact on the sedimentary record. *Biogeosciences*, 7, 483–511. <https://doi.org/10.5194/bg-7-483-2010>